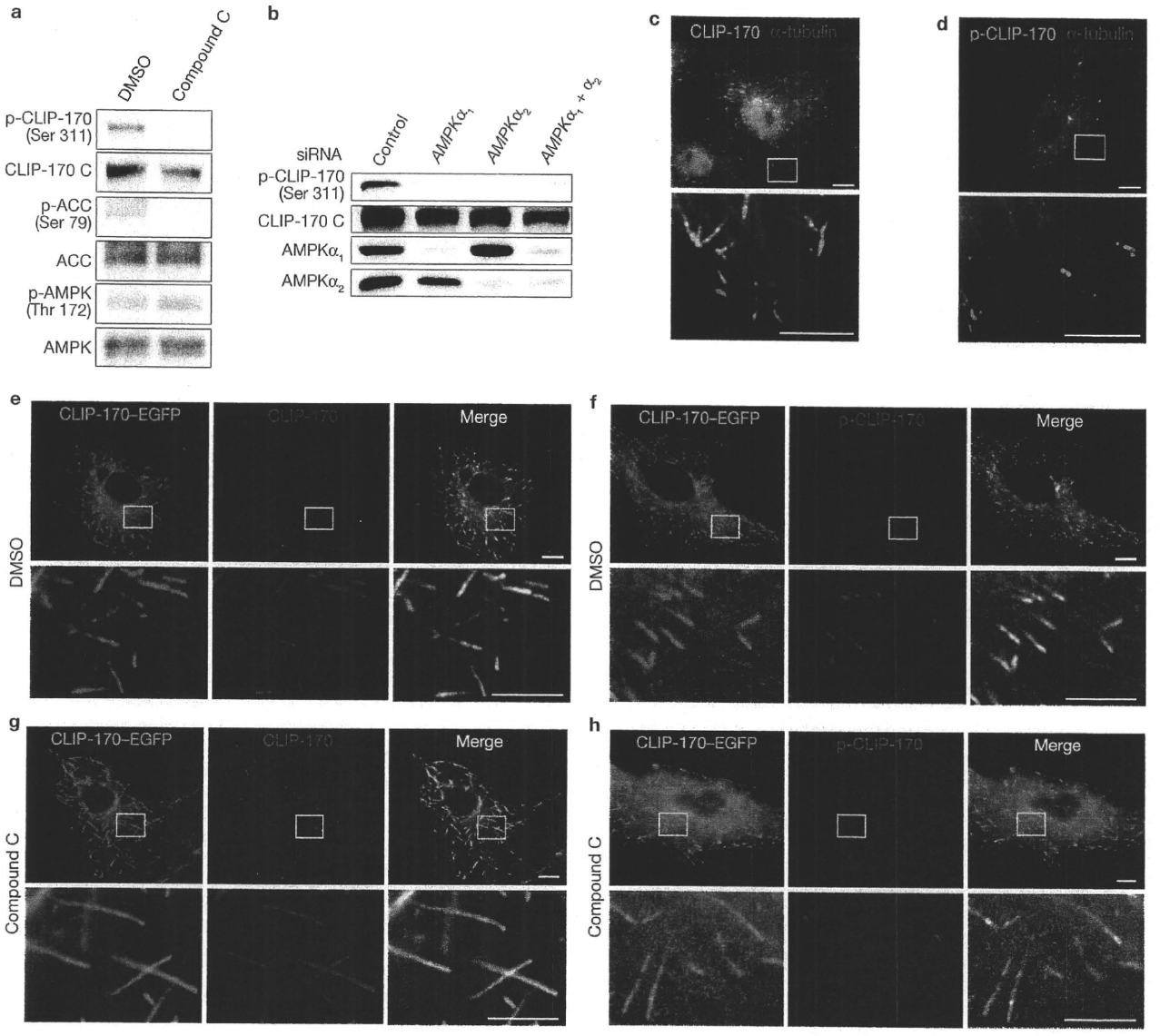

Figure 2 CLIP-170 phosphorylated by AMPK localizes to microtubule tips. (**a**) Immunoblot analysis of the phosphorylation level of CLIP-170, AMPK, and ACC in cells treated with 0.2% DMSO or Compound C (20 μM). CLIP-170 C is a non-phosphospecific antibody that recognizes the C terminus of CLIP-170. (**b**) Immunoblot analysis of the phosphorylation level of CLIP-170 and the expression level of AMPKα_1 and α_2 in cells treated with siRNA targeting *AMPK*α_1, α_2, or both subunits of AMPK. (**c**) Immunostained images of Vero cells stained with anti-α-tubulin and the anti-CLIP-170 C antibodies. (**d**) Immunostained images of Vero cells stained with α-tubulin and p-CLIP-170 antibodies. (**e**, **f**) Immunostained images of Vero cells stably expressing CLIP-170–EGFP (GFP image, left) and treated with DMSO as a control. These cells were stained with a CLIP-170 C antibody (**e**, centre) or a p-CLIP-170 antibody (**f**, centre). (**g**, **h**) Immunostained images of Vero cells stably expressing CLIP-170–EGFP (GFP image, left) and treated with Compound C. These cells were stained with a CLIP-170 C antibody (**g**, centre) or a p-CLIP-170 antibody (**h**, centre). The merged images of each panel are shown on the right. The white boxed regions in the panels are enlarged below each panel. Scale bars, 10 μm (**c**–**h**, upper rows) and 5 μm (**c**–**h**, bottom rows). Uncropped images of blots are shown in Supplementary Information, Fig. S5.

spot within the CLIP-170–EGFP-positive region (Fig. 2h, red or yellow). Most of the CLIP-170 on microtubules, therefore, was non-phosphorylated, and a small amount of phosphorylated CLIP-170 accumulated at the distal ends. To examine the precise distribution of CLIP-170 on the microtubules under AMPK-inhibited conditions, linescan analysis along the microtubules was performed using double immunocytochemistry with CLIP-170 C and tubulin antibodies. We separately measured total CLIP-170 associated with microtubule plus ends, and CLIP-170 associated with the outermost microtubule tips (within a 0.129-μm square box at the very end of the microtubules). When compared with the DMSO control Compound C treatment increased the association of CLIP-170 with microtubules both in the whole tip (6-fold) and at the outer tip (1.7-fold) (Supplementary Information, Fig. S2b–d). Depletion of both AMPKα_1 and α_2 by siRNA also resulted in accumulation of CLIP-170 on microtubule plus ends, similarly to inhibition by Compound C (Supplementary Information, Fig. S2e, f). This characteristic change of CLIP-170 localization prompted us to examine the role of AMPK in the regulation of microtubule dynamics.

To study how AMPK regulates microtubule dynamics, we examined the behaviour of CLIP-170 in living cells. First, we tested whether phosphorylation levels of CLIP-170 affected polymerization of microtubules.

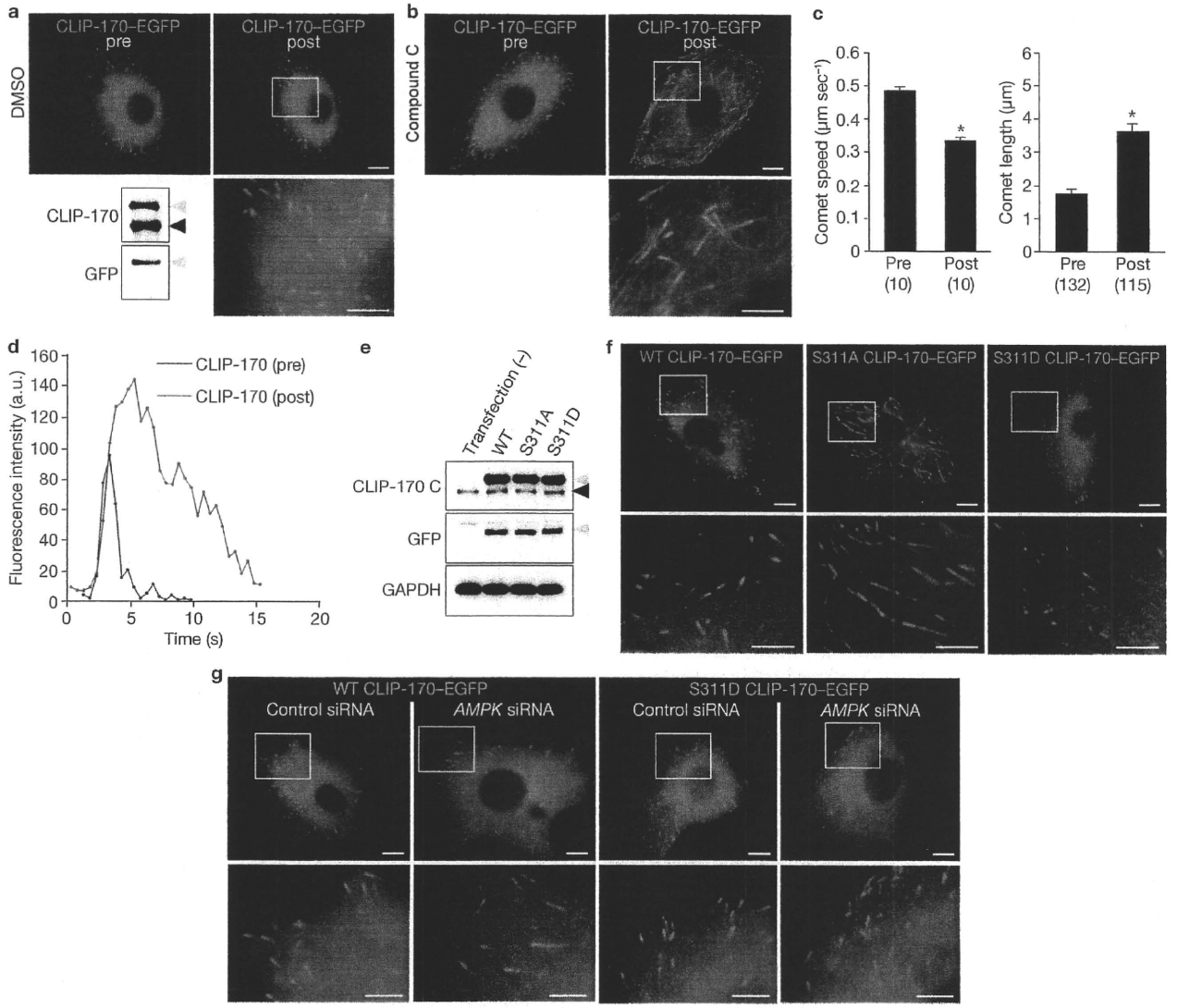

Figure 3 AMPK-phosphorylated CLIP-170 regulates microtubule dynamics. (**a**, **b**) GFP images of Vero cells stably expressing CLIP-170–EGFP before (pre) and 10 min after (post) treatment with 0.2% DMSO control (**a**) or Compound C (20 μM, **b**). The immunoblot on the left shows exogenous CLIP-170–EGFP (grey arrowheads) and endogenous CLIP-170 (black arrowhead). (**c**) Bar graphs showing the speed (left panel) and length (right panel) of a single comet before (pre) and 10 min after (post) Compound C treatment in the same cell. Values are means ± s.e.m.; *n* shown in parentheses; $^*P < 0.01$, compared with pre. (**d**) Fluorescence intensity plots of CLIP-170–EGFP of the same cell before (pre, blue) and 10 min after (post, red) Compound C treatment. (**e**) Expression levels of wild-type (WT), S311A and S311D CLIP-170–EGFP in transiently transfected Vero cells were comparable, as determined by immunoblotting using the antibodies indicated on the left. The grey and black arrowheads indicate GFP-tagged exogenous CLIP-170 and endogenous CLIP-170, respectively. (**f**) GFP images of cells transiently expressing WT (left), S311A (centre) and S311D (right) CLIP-170–EGFP. (**g**) GFP images of the cells transiently expressing WT and S311D CLIP-170–EGFP treated with control siRNA or siRNA targeting both *AMPK*α_1 and α_2. White boxed regions in the panels are enlarged below each panel. Scale bars, 10 μm (**a**, **b**, **f**, **g**, upper panels) and 5 μm (**a**, **b**, **f**, **g**, enlarged images). Uncropped images of blots are shown in Supplementary Information, Fig. S5.

By live-cell imaging, we observed that stably expressed CLIP-170–EGFP accumulated at the distal ends of microtubules and seemed to move like a comet from the centrosome to the cell periphery (as shown in sequential images converted to video, Supplementary Information, Movie 1). The speed of the CLIP-170 comets coincided with that of microtubule polymerization[16,17]. Consistent with our results in fixed cells (Fig. 2), 10-min inhibition of AMPK by Compound C in living cells also resulted in elongated CLIP-170 comets, compared with control DMSO-treated cells (Fig. 3a–c). Moreover, the speed of the comets was reduced by Compound C (Fig. 3c; Supplementary Information, Movie 2). To analyse the CLIP-170 behaviour more precisely, we measured the fluorescence intensity values along the CLIP-170–EGFP tracks over time in the same living cells before and 10 min after Compound C treatment. This fluorescence intensity analysis of CLIP-170–EGFP demonstrated that Compound C markedly increased the peak fluorescence intensity and slowed the dissociation of CLIP-170 from the older part of the microtubules (Fig. 3d). Using the same cell line stably expressing CLIP-170–EGFP, depletion of AMPK by siRNA also reduced the speed of the comets and increased the length of CLIP-170 comets (Supplementary Information, Fig. S2g–i, Movie 3). To elucidate the specific role of CLIP-170 Ser 311 phosphorylation by AMPK, we compared the phenotypes of cells transiently transfected with wild-type and two Ser 311 mutants of CLIP-170. S311A CLIP-170–EGFP

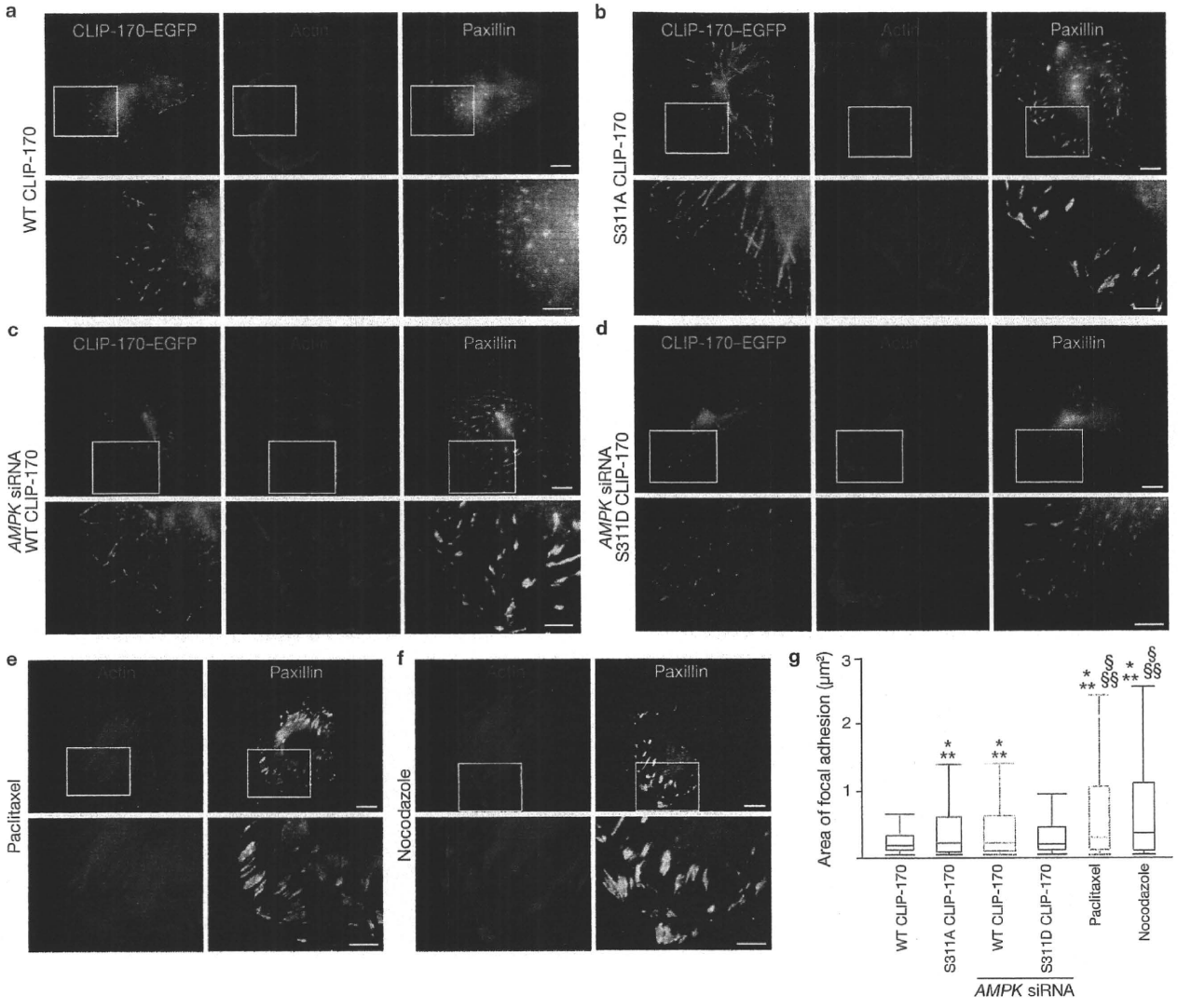

Figure 4 Loss of CLIP-170 phosphorylation increases the size of focal adhesions. (**a**, **b**) Immunostained images of Vero cells transiently expressing wild-type (WT; **a**) and S311A (**b**) CLIP-170–EGFP (GFP image, left). These cells were stained with fluorescein-conjugated phalloidin (centre) and a paxillin antibody (right) to visualize actin microfilaments and focal adhesions, respectively. (**c**, **d**) Immunostained images of Vero cells transiently expressing WT (**c**) and S311D (**d**) CLIP-170–EGFP (GFP image, left) treated with siRNA targeting both *AMPK*α_1 and α_2. These cells were stained with fluorescein-conjugated phalloidin (centre) and a paxillin antibody (right). (**e**, **f**) Immunostained images of Vero cells treated with 5 μM paclitaxel (**e**) or 10 μM nocodazole (**f**). These cells were stained with fluorescein-conjugated phalloidin (left) and a paxillin antibody (right). The white boxed regions in the panels are enlarged below each panel. Scale bars, 10 μm (**a**–**f**, upper row) and 5 μm (**a**–**f**, bottom row). (**g**) Box and whisker plots of the area stained with a paxillin antibody showing the 25th percentile (bottom line of each box), median (middle line of each box), 75th percentile (top line of each box), and the 5th and 95th percentiles (each whisker); $n = 10$ for each group; $^{*}P < 0.01$, compared with WT CLIP-170; $^{**}P < 0.01$, compared with S311D CLIP-170 treated with *AMPK* siRNA; $^{\S}P < 0.01$, compared with S311A CLIP-170; $^{\S\S}P < 0.01$, compared with WT CLIP-170 treated with *AMPK* siRNA.

is a non-phosphorylatable mutant, and a Ser 311-to-Asp mutant (S311D CLIP-170–EGFP) is a phosphomimetic mutant. These EGFP fusion proteins were equally expressed in Vero cells (Fig. 3e). S311A CLIP-170–EGFP accumulated as comets with longer tails and moved more slowly than wild-type CLIP-170–EGFP (Fig. 3f centre; Supplementary Information, Table S1, Movie 4). By contrast, S311D CLIP-170–EGFP had the same comet length and moved with the same speed as wild-type CLIP-170–EGFP (Fig. 3f, right; Supplementary Information, Table S1, Movie 5). These findings are consistent with the observation that most of the endogenous CLIP-170 was phosphorylated by AMPK. Furthermore, S311D CLIP-170–EGFP rescued the phenotypes caused by siRNA depletion of AMPK (Fig. 3g; Supplementary Information, Table S1, Movie 6). Also, in the cells treated with Compound C, transfection of S311D CLIP-170–EGFP restored comet speed and length. Quantitative data of comet speed and length in various conditions are summarized in Supplementary Information, Table S1.

CLIP-170 binds only to the growing phase of microtubules. To further examine microtubule dynamics during the shortening phase, Vero cells stably expressing α-tubulin–EGFP were observed before and 10 min after Compound C treatment. Compound C markedly decreased the microtubule shortening distance (Supplementary Information, Fig. S2j, Movie 7). This change in microtubule behaviour may stabilize microtubules. We then observed microtubule stability by staining them with an antibody against detyrosinated tubulin (Glu tubulin,

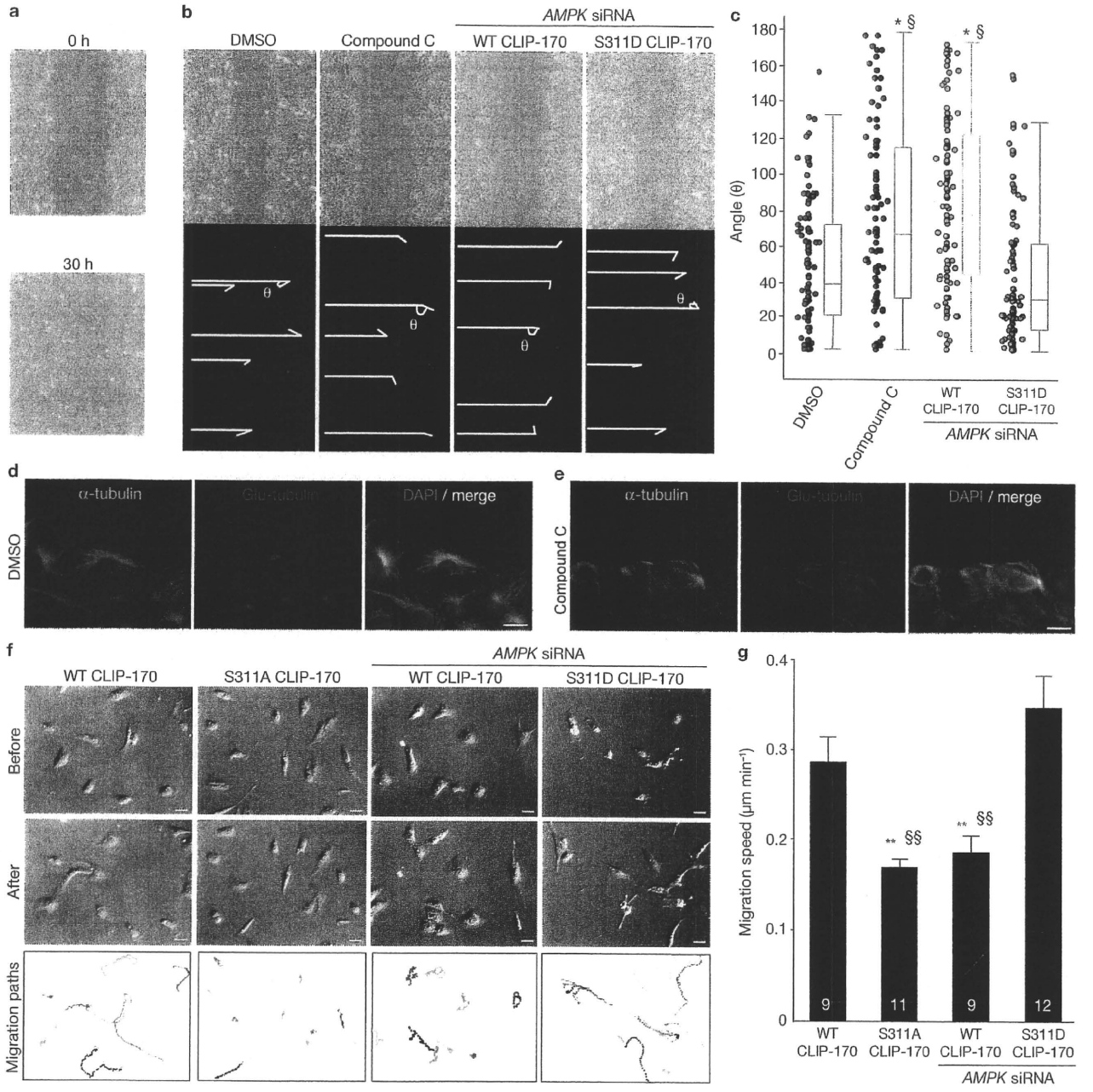

Figure 5 Phosphorylation of CLIP-170 at Ser 311 is essential for cell polarity and directional cell migration. (**a**) Phase contrast microscopy images of Vero cells before (upper panel) and 30 h after (lower panel) scratch. (**b**) Phase contrast microscopy images (upper panels) and immunostained images of Vero cells stained with a γ-tubulin antibody (lower panels) after being subjected to a scratch assay. Images were captured 12 h after incubation. The cells were treated by either repeated administration of DMSO control or Compound C, or transiently transfected with wild-type (WT) or S311D CLIP-170 and siRNA targeting both *AMPK*α_1 and α_2. To assess cell polarity, the angles (θ) between the lines of γ-tubulin and the scratched line at the centre of each nucleus were measured as a marker for MTOC reorientation (lower panels). (**c**) Box and whisker plots of angles (θ) with actual data points shown on the left; n=100 per group; $^{*}P$ <0.01, compared with DMSO; $^{\S}P$ <0.01, compared with S311D CLIP-170 treated with *AMPK* siRNA. (**d**, **e**) Images of Vero cells immunostained with an α-tubulin (left, green) and a detyrosinated (Glu) tubulin antibody (centre, red) after being subjected to a scratch assay following repeated treatment with control DMSO (**d**) or Compound C (**e**) for 6 h. DAPI stained nucleus (blue). The merged images of each panel are shown on the right. Scale bars, 20 μm. (**f**) Time lapse images acquired by differential interference contrast of cells transiently expressing WT, S311A, and WT or S311D CLIP-170 treated with siRNA targeting both *AMPK*α_1 and α_2. Images acquired before (upper line of each panel) and after 12 h (middle line of each panel) are shown. The bottom row of each panel shows the individual paths of migrating cells over 12 h. Scale bars, 30 μm. (**g**) Bar graphs showing the migration speed of the cells from (**f**); Numbers in the bars indicate n. Values represent means ± s.e.m; $^{**}P$ <0.01, compared with WT CLIP-170. $^{\S\S}P$ <0.01, compared with S311D CLIP-170 treated with *AMPK* siRNA.

named for the newly exposed C-terminal glutamate residue). The amount of stable microtubules was greater in cells transiently expressing S311A CLIP-170–EGFP (Supplementary Information, Fig. S3b) than in cells transiently expressing wild-type CLIP-170 (Supplementary Information, Fig. S3a). Cell depleted of AMPK by siRNA (Supplementary Information, Fig. S3g), or treated with Compound C (Supplementary

Information, Fig. S3d) also showed the same phenotype as cells expressing S311A CLIP-170. These phenotypes were rescued by S311D CLIP-170 (Supplementary Information, Fig. S3f, i). Collectively, these data suggest that phosphorylation of CLIP-170 at Ser 311 by AMPK is necessary for proper CLIP-170 dissociation from microtubules, and that this modification of CLIP-170 is essential for efficient polymerization and depolymerization of microtubules. Dynamic modulation of microtubule polymerization and stability by AMPK-phosphorylated CLIP-170 might represent a previously unknown mechanism through which AMPK establishes cell polarity. Therefore, we further examined the role of CLIP-170 phosphorylation by AMPK during cell polarization and subsequent cell migration.

During cell migration, microtubules target focal adhesions and regulate cell–extracellular matrix (ECM) adhesion[18–20]. Thus, we first examined whether phosphorylation of CLIP-170 at Ser 311 affects the size of focal adhesions. Isolated Vero cells transiently expressing wild-type CLIP-170–EGFP formed an actin meshwork in protruding lamellipodium. Furthermore, staining focal adhesions with a paxillin antibody revealed small, scattered spots located predominantly at the protruding lamellipodium (Fig. 4a). By contrast, expression of S311A CLIP-170–EGFP caused loss of lamellipodium formation and adhesion maturation, which resulted in significantly enlarged spots (Fig. 4b). Similar phenotypes were observed when AMPK was depleted by siRNA (Fig. 4c) or inhibited by Compound C (Supplementary Information, Fig. S4b). These AMPK depletion phenotypes were almost completely rescued by the expression of S311D CLIP-170–EGFP (Fig. 4d, g; Supplementary Information, Fig. S4d). Treatment with paclitaxel and nocodazole (Fig. 4e, f), both of which disturb microtubule dynamics, resulted in similar phenotypes of abnormal size of focal adhesion as cells expressing S311A CLIP-170–EGFP and cells depleted of AMPK. These data indicate that AMPK-dependent phosphorylation of CLIP-170 regulates the size of focal adhesions by regulating microtubule dynamics. The fact that inhibiting AMPK-induced phosphorylation of CLIP-170 altered the size of focal adhesions and lamellipodium formation suggests an important role of the AMPK–CLIP-170 signalling axis in cell polarity and migration. We examined the effect of AMPK inhibition on cell polarity using the scratch assay. The leading cells started to polarize and migrated towards a scratched line, closing the gap in about 30 h (Fig. 5a). However, repeated treatment with Compound C and depletion of AMPK by siRNA both inhibited closure of the gap and interfered with microtubule-organizing centre (MTOC) reorientation in leading cells. Expression of S311D CLIP-170 rescued AMPK depletion (Fig. 5b, c; Supplementary Information, Fig S4g, h). The first two layers of the leading cells showed that the stabilized microtubules stained with a detyrosinated (anti-Glu) tubulin antibody were clearly polarized towards the leading edge (Fig. 5d). By contrast, AMPK inhibition by Compound C increased the amount of stable microtubules, which lost their orientation towards the leading edge (Fig. 5e). Finally, we tested the effect of CLIP-170 phosphorylation on free cell migration. Wild-type CLIP-170-expressing cells migrated with active lamellipodium formation. By contrast, S311A CLIP-170-expressing cells and wild-type CLIP-170-expressing cells treated with *AMPK* siRNA showed diminished migration and fewer membrane extensions (Fig. 5f). Again, expression of S311D CLIP-170 rescued the effect of siRNA *AMPK* knockdown of (Fig. 5g; Supplementary Information, Movie 8). These data suggest that AMPK-induced phosphorylation of CLIP-170 is required to establish front–rear polarity and proper cell migration, presumably through the regulation of microtubule tip dynamics.

We have shown here that CLIP-170 is a strong candidate AMPK substrate that regulates cell polarity through alteration of its dynamics on the plus ends of microtubules. Recently, abnormal mitotic phenotypes were observed for both *AMPK*- and *LKB1*-null *Drosophila*. They demonstrated that AMPK phosphorylates myosin regulatory light chain (MRLC) directly, and a phosphomimetic MRLC transgene rescued the polarity phenotypes induced by loss of the AMPK pathway[6]. However, the transgene did not rescue all phenotypes, suggesting that AMPK signalling is mediated by additional downstream targets.

The dynamics of CLIP-170 on microtubules were recently and precisely investigated both *in vitro* and *in vivo*[13,17]. In these reports, CLIP-170 turnover on microtubules was rapid, and the diffusion of CLIP-170 was rate-limiting for its binding to microtubule plus ends. They also showed that the ends of growing microtubules contain a surplus of sites to which CLIP-170 can bind, and the older lattice has a lower affinity for CLIP-170 than the newer, growing ends of the microtubules. These changes in the affinity of plus end proteins for microtubules may be essential for their effects on microtubule dynamics.

We could not demonstrate an altered affinity of phosphorylated CLIP-170 for the microtubule plus end *in vitro* because of the difficulty associated with reconstituting the plus end as *in vivo*. However, we speculate, for the following reasons, that non-phosphorylated CLIP-170 increased its affinity to microtubules. First, linescan analysis showed that depletion of AMPK activity increased the association not only of total CLIP-170 with the microtubule but also of CLIP-170 at the outer tip. Second, the fluorescence intensity analysis measured in living cells indicated that non-phosphorylated CLIP-170 increased the peak fluorescence intensity and slowed its dissociation from the plus end of microtubules. Third, phosphorylated CLIP-170 localized within the more distal portion of the total CLIP-170 population. These results support the hypothesis that the phosphorylation status of CLIP-170 at Ser 311 determines its affinity for microtubules. Because CLIP-170 turnover on microtubules is rapid, phosphorylation may be a suitable modification to regulate its affinity for microtubules. We conclude that phosphorylation of CLIP-170 alters its affinity for microtubule plus ends and that this phenomenon might contribute to the rapid turnover of CLIP-170, which is necessary for efficient microtubule polymerization.

The observation that the phosphorylation status of CLIP-170 regulates the growth rate of microtubules has not been reported. The precise mechanisms remain unclear; however we speculate that Ser 311 phosphorylation is necessary to reduce the affinity of CLIP-170 for the microtubule lattice and promote the efficient turnover of CLIP-170 at the plus end, similarly to a microtubule polymerase.

Another intriguing phenotype of AMPK depletion is the marked enhancement of microtubule stabilization in migrating cells. Moreover, AMPK depletion impaired the polarized stabilization of microtubules towards the leading edge. AMPK depletion not only reduced the speed of polymerization but also decreased the shortening distance of microtubules. Because both phenomena prolong the lifetime of microtubules, these two changes might cause the ubiquitous enhancement of microtubule stabilization.

Expression of the non-phosphorylatable CLIP-170 S311A mutant and depletion of AMPK disrupted front–rear polarity and reduced cell migration. The precise mechanisms of this phenotype are unclear, but decreased

microtubule polymerization and unpolarized microtubule stabilization might affect the function of microtubules, which are required to establish cell polarity. We have shown that inhibiting CLIP-170 phosphorylation resulted in significant enlargement of focal adhesions, as detected with a paxillin antibody. Enlarged focal adhesions are similar to the phenotype observed in cells treated with paclitaxel or nocodazole, both of which disrupt microtubule dynamics. Microtubules bind to paxillin and help the cell adhesion system to destabilize focal adhesions and promote cell motility[21,22]. These functions suggest that microtubules play a key part in cell polarity and migration through interactions with focal adhesion molecules. Taken together, the results suggest that AMPK promotes the appropriate formation of focal adhesions, the subsequent establishment of cell polarity, and directional cell migration through efficient polymerization of microtubules, by phosphorylating CLIP-170 at Ser 311.

Under normal cell culture conditions, neither enhanced activation of AMPK by AICAR nor S311D CLIP-170–EGFP altered microtubule dynamics, indicating a high basal phosphorylation of CLIP-170. This might be caused by a high affinity of AMPK for CLIP-170, or colocalization of AMPK and CLIP-170.

The results of our broad substrate screening method suggest that CLIP-170 is one of the most important substrates of AMPK in various organs. We believe that observing microtubule dynamics is necessary to evaluate multiple functions of AMPK. Also, similarly to paclitaxel or nocodazole treatment, strong inhibition of microtubule dynamics by the CLIP-170 S311A mutant may have clinical implications. The interaction between AMPK and CLIP-170 might be a therapeutic target for treatment of conditions such as cancer, tumour angiogenesis and neointimal hyperplasia. □

METHODS

Methods and any associated references are available in the online version of the paper at http://www.nature.com/naturecellbiology/

Note: Supplementary Information is available on the Nature Cell Biology website.

ACKNOWLEDGEMENTS

We thank M. Amano and S. Fukuhara for helpful discussions, and M. Koyama (Olympus Corporation) for technical advice regarding microscopy. This research was supported by: a Grants-in-Aid from the Ministry of Health, Labour and Welfare of Japan; Grants-in-Aid from the Ministry of Education, Culture, Sports, Science and Technology of Japan; grants from the Japan Heart Foundation; grants from the Japan Cardiovascular Research Foundation; a grant from the Japan Society for the Promotion of Science; a grant from the Mochida Memorial Foundation for Medical and Pharmaceutical Research; and a Grant-in-Aid from the Japan Medical Association.

AUTHOR CONTRIBUTIONS

A.N. designed and conducted the study, performed most of the experiments, and wrote the manuscript; S.T. designed and conducted the study, performed the biochemical experiments and wrote the manuscript; H.K. carried out immunoblot analysis; K.M. independently counted the number of cells; S.Y. helped to generate the plasmids; Y.A., O.S., S.H., Y.S., H.A., M.A. and T.M. discussed the results and reviewed the manuscript; T.W. and K.K. generated and provided antibodies and Vero cells and reviewed the manuscript; N.M. conducted and supported the biological experiments and wrote the manuscript; M.K. supervised all work.

COMPETING INTERESTS

The authors declare no competing financial interests.

Published online at http://www.nature.com/naturecellbiology/
Reprints and permissions information is available online at http://npg.nature.com/reprintsandpermissions/

1. Yeh, L. A., Lee, K. H. & Kim, K. H. Regulation of rat liver acetyl-CoA carboxylase. Regulation of phosphorylation and inactivation of acetyl-CoA carboxylase by the adenylate energy charge. *J. Biol. Chem.* **255**, 2308–2314 (1980).
2. Hardie, D. G. AMP-activated/SNF1 protein kinases: conserved guardians of cellular energy. *Nature Rev. Mol. Cell Biol.* **8**, 774–785 (2007).
3. Zhang, L., Li, J., Young, L. H. & Caplan, M. J. AMP-activated protein kinase regulates the assembly of epithelial tight junctions. *Proc. Natl Acad. Sci. USA* **103**, 17272–17277 (2006).
4. Zheng, B. & Cantley, L. C. Regulation of epithelial tight junction assembly and disassembly by AMP-activated protein kinase. *Proc. Natl Acad. Sci. USA* **104**, 819–822 (2007).
5. Mirouse, V., Swick, L. L., Kazgan, N., St. Johnston, D. & Brenman, J. E. LKB1 and AMPK maintain epithelial cell polarity under energetic stress. *J. Cell Biol.* **177**, 387–392 (2007).
6. Lee, J. H. *et al.* Energy-dependent regulation of cell structure by AMP-activated protein kinase. *Nature* **447**, 1017–1020 (2007).
7. Williams, T. & Brenman, J. E. LKB1 and AMPK in cell polarity and division. *Trends Cell Biol.* **18**, 193–198 (2008).
8. Jansen, M., Ten Klooster, J. P., Offerhaus, G. J. & Clevers, H. LKB1 and AMPK family signaling: the intimate link between cell polarity and energy metabolism. *Physiol. Rev.* **89**, 777–798 (2009).
9. Martin, S. G. & St. Johnston, D. A role for *Drosophila* LKB1 in anterior–posterior axis formation and epithelial polarity. *Nature* **421**, 379–384 (2003).
10. Watts, J. L., Morton, D. G., Bestman, J. & Kemphues, K. J. The *C. elegans par-4* gene encodes a putative serine-threonine kinase required for establishing embryonic asymmetry. *Development* **127**, 1467–1475 (2000).
11. Rickard, J. E. & Kreis, T. E. Identification of a novel nucleotide-sensitive microtubule-binding protein in HeLa cells. *J. Cell Biol.* **110**, 1623–1633 (1990).
12. Pierre, P., Scheel, J., Rickard, J. E. & Kreis, T. E. CLIP-170 links endocytic vesicles to microtubules. *Cell* **70**, 887–900 (1992).
13. Dragestein, K. A. *et al.* Dynamic behavior of GFP-CLIP-170 reveals fast protein turnover on microtubule plus ends. *J. Cell Biol.* **180**, 729–737 (2008).
14. Hardie, D. G., Carling, D. & Carlson, M. The AMP-activated/SNF1 protein kinase subfamily: metabolic sensors of the eukaryotic cell? *Annu. Rev. Biochem.* **67**, 821–855 (1998).
15. Bain, J. *et al.* The selectivity of protein kinase inhibitors: a further update. *Biochem. J.* **408**, 297–315 (2007).
16. Perez, F., Diamantopoulos, G. S., Stalder, R. & Kreis, T. E. CLIP-170 highlights growing microtubule ends *in vivo*. *Cell* **96**, 517–527 (1999).
17. Bieling, P. *et al.* CLIP-170 tracks growing microtubule ends by dynamically recognizing composite EB1/tubulin-binding sites. *J. Cell Biol.* **183**, 1223–1233 (2008).
18. Wu, X., Kodama, A. & Fuchs, E. ACF7 regulates cytoskeletal-focal adhesion dynamics and migration and has ATPase activity. *Cell* **135**, 137–148 (2008).
19. Rodriguez, O. C. *et al.* Conserved microtubule–actin interactions in cell movement and morphogenesis. *Nat. Cell Biol.* **5**, 599–609 (2003).
20. Small, J. V., Geiger, B., Kaverina, I. & Bershadsky, A. How do microtubules guide migrating cells? *Nature Rev. Mol. Cell Biol.* **3**, 957–964 (2002).
21. Turner, C. E. Paxillin and focal adhesion signalling. *Nat. Cell Biol.* **2**, E231–E236 (2000).
22. Broussard, J. A., Webb, D. J. & Kaverina, I. Asymmetric focal adhesion disassembly in motile cells. *Curr. Opin. Cell Biol.* **20**, 85–90 (2008).

Ablation of C/EBP Homologous Protein Attenuates Endoplasmic Reticulum–Mediated Apoptosis and Cardiac Dysfunction Induced by Pressure Overload

Hai Ying Fu, MD, PhD; Ken-ichiro Okada, MD, PhD; Yulin Liao, MD, PhD; Osamu Tsukamoto, MD, PhD; Tadashi Isomura, MD, PhD; Mitsutoshi Asai, MD, PhD; Tamaki Sawada, MD, PhD; Keiji Okuda, MD; Yoshihiro Asano, MD, PhD; Shoji Sanada, MD, PhD; Hiroshi Asanuma, MD, PhD; Masanori Asakura, MD, PhD; Seiji Takashima, MD, PhD; Issei Komuro, MD, PhD; Masafumi Kitakaze, MD, PhD; Tetsuo Minamino, MD, PhD

Background—Apoptosis may contribute to the development of heart failure, but the role of apoptotic signaling initiated by the endoplasmic reticulum in this condition has not been well clarified.

Methods and Results—In myocardial samples from patients with heart failure, quantitative real-time polymerase chain reaction revealed an increase in messenger RNA for C/EBP homologous protein (CHOP), a transcriptional factor that mediates endoplasmic reticulum–initiated apoptotic cell death. We performed transverse aortic constriction or sham operation on wild-type (WT) and CHOP-deficient mice. The CHOP-deficient mice showed less cardiac hypertrophy, fibrosis, and cardiac dysfunction compared with WT mice at 4 weeks after transverse aortic constriction, although the contractility of isolated cardiomyocytes from CHOP-deficient mice was not significantly different from that in the WT mice. In the hearts of CHOP-deficient mice, phosphorylation of eukaryotic translation initiation factor 2α, which may reduce protein translation, was enhanced compared with WT mice. In the hearts of WT mice, CHOP-increased apoptotic cell death with activation of caspase-3 was observed at 4 weeks after transverse aortic constriction. In contrast, CHOP-deficient mice had less apoptotic cell death and lower caspase-3 activation at 4 weeks after transverse aortic constriction. Furthermore, the Bcl2/Bax ratio was decreased in WT mice, whereas this change was significantly blunted in CHOP-deficient mice. Real-time polymerase chain reaction microarray analysis revealed that CHOP could regulate several Bcl2 family members in failing hearts.

Conclusions—We propose the novel concept that CHOP, which may modify protein translation and mediate endoplasmic reticulum–initiated apoptotic cell death, contributes to development of cardiac hypertrophy and failure induced by pressure overload. (***Circulation.*** **2010;122:361-369.**)

Key Words: apoptosis ■ endoplasmic reticulum ■ heart failure ■ hypertrophy

The endoplasmic reticulum (ER) is classically characterized as an organelle that participates in the folding of membrane proteins and secretory proteins.[1,2] Various cellular stresses, including ischemia, hypoxia, heat shock, genetic mutation, oxidative stress, and increased protein synthesis, can lead to impairment of ER function.[1,2] Stimuli that cause ER dysfunction are collectively known as ER stress. When ER stress occurs, various ER stress sensor proteins activate a transcriptional and translational response that is known as the unfolded protein response to cope with the accumulation of unfolded or misfolded proteins in the ER lumen.[1,2] After the onset of ER stress, eukaryotic translation initiation factor 2α (eIF2α) is phosphorylated to repress global protein synthesis.[1,2] When ER stress is excessive and/or prolonged, however, apoptotic signals are initiated by the ER, including induction of C/EBP homologous protein (CHOP), activation of Jun N-terminal kinase (JNK), and cleavage of caspase-12.[3–5]

Clinical Perspective on p 369

Previous studies have demonstrated the morphological development of the ER in hypertrophic and failing human hearts.[6] Because the morphological development of the ER indicates the overload to the ER,[7,8] the unfolded protein response should occur in diseased hearts. However, the

Received November 6, 2009; accepted May 19, 2010.

From the Department of Cardiovascular Medicine, Osaka University Graduate School of Medicine, Suita, Osaka, Japan (H.Y.F., K.-i.O., O.T., M.A., T.S., K.O., Y.A., S.T., I.K., T.M.); Department of Cardiovascular Surgery, Hayama Heart Center, Shimoyamaguchi, Hayama, Kanagawa, Japan (T.I.); Department of Cardiovascular Medicine, National Cerebral and Cardiovascular Center, Suita, Osaka, Japan (S.S., H.A., M.A., M.K.); China-Japan Collaborative Laboratory of Cardiovascular Physiology, Department of Pathophysiology, Southern Medical University, Guangzhou, China (Y.L.).

The online-only Data Supplement is available with this article at http://circ.ahajournals.org/cgi/content/full/CIRCULATIONAHA.109.917914/DC1.

Correspondence to Tetsuo Minamino, MD, PhD, Department of Cardiovascular Medicine, Osaka University Graduate School of Medicine, 2–2 Yamadaoka, Suita, Osaka 565-0871, Japan. E-mail minamino@cardiology.med.osaka-u.ac.jp

Circulation **is available at http://circ.ahajournals.org** **DOI: 10.1161/CIRCULATIONAHA.109.917914**

molecular signaling mechanisms involved in the unfolded protein response have not been fully identified in diseased hearts. Recently, we have demonstrated that expression of ER chaperones was increased and CHOP was induced in experimental heart failure.[9] CHOP has been identified as an ER-initiated proapoptotic signal that plays an important role in the pathophysiology of diabetes mellitus and neurodegenerative diseases.[3,10,11] Furthermore, CHOP can also directly regulate death effectors such as Bcl2, which is one of key determinants of cell death or survival.[12] Although the apoptosis of cardiomyocytes may contribute to the development of heart failure,[13–16] the role of ER-initiated apoptosis in the pathophysiology of heart failure remains unclear. In the present study, we investigated ER stress signaling in human hearts. We also performed in vivo studies to clarify the pathophysiological role of CHOP in the development of cardiac hypertrophy and failure and examined the potential downstream signaling of CHOP in pressure-overloaded hearts of mice.

Methods

Materials

Antibodies for CHOP, Bax, Bcl2, ATF4, ATP5α, and actin were obtained from Santa Cruz Biotechnology (Santa Cruz, Calif); antibodies for phospho-SAPK/JNK, SAPK/JNK, phospho-eIF2α, eIF2α, and cleaved caspase-3 were obtained from Cell Signaling Technology, Inc (Danvers, Mass). Isoproterenol and the antibody for caspase-12 were obtained from Sigma Chemical Corp (St. Louis, Mo). Antibodies for BiP and GAPDH were purchased from Assay Designs, Inc (Ann Arbor, Mich) and Millipore Corp (Billerica, Mass), respectively.

Human Heart Samples

Human heart samples were studied according to the protocol approved by the Institutional Review boards of the National Cardiovascular Center (No. 14 to 18) and Hayama Heart Center. For quantitative real-time reverse-transcription polymerase chain reaction (PCR), we used surgical samples of myocardium removed from 12 patients with dilated cardiomyopathy and 3 patients with ischemic cardiomyopathy who underwent left ventriculoplasty at the Hayama Heart Center. Six control heart samples for quantitative real-time PCR were obtained from BD Biosciences (San Jose, Calif). Tissues were frozen at −80°C until use for extraction of RNA.

Animal Preparation

Mice lacking the *CHOP* gene were generated on a C57BL/6 background as described previously.[17] Experiments were performed with CHOP-deficient mice and littermate control mice. All procedures were done in accordance with the guiding principles of Osaka University School of Medicine with regard to animal care and the "Position of the American Heart Association on Research Animal Use."

Transverse Aortic Constriction

Pressure overload of the heart was induced in 10-week-old male mice (20 to 25 g) by transverse aortic constriction (TAC) as described previously.[18,19]

Immunohistological Analysis

Immunohistological analysis was performed as described previously.[18,19]

Echocardiography

Cardiac function was assessed by Doppler echocardiography with a 15-MHz transducer (Philips, SONOS5500, Eindhoven, the Netherlands).[18,19]

Preparation of Neonatal Rat Cardiomyocytes

Primary cardiomyocyte cultures were prepared from neonatal rat hearts.[20] We used short interfering RNA (siRNA) (cocktail containing equal amounts of the 3 types of siRNA—5′-CGAAGAGGAAGAAUCAAA-3′, 5′-GGAAACAGCGACUGAAGGA-3′, and 5′-GGGACUGAGGGUAGACCAA-3′)—to knock down *CHOP* messenger RNA (mRNA) as described previously.[20] Cardiomyocytes were stained with rhodamine-phalloidin (Invitrogen Corp, Carlsbad, Calif).

Measurement of Contractility With Isolated Adult Mice Cardiomyocytes

Adult cardiomyocytes were isolated from 8-week-old wild-type (WT) or CHOP knockout mice and were stored in Hanks buffer (Invitrogen Corp) containing 1.2 mmol/L $CaCl_2$. Field stimulation at 1-Hz pacing rate was done with 5-ms square pulses of constant voltage at 20% above threshold.[21] Changes in cell length during contracting and relaxing were recorded with an inverted microscopy (Olympus IX81, Olympus Corp, Tokyo, Japan) and analyzed with Metamorph software (Molecular Devices Corp, Tokyo, Japan). Cell shortening was calculated as follows: (relaxing length−contracting length)/relaxing length.

Quantitative Real-Time PCR

Quantitative real-time PCR of human heart tissue was performed according to the Omniscript Reverse Transcription Handbook (Qiagen Inc, Valencia, Calif). The primers and probes used for quantification of *BiP*, *ATF4*, *CHOP*, and *GAPDH* were all designed according to the manufacturer's protocol (Applied Biosystems, Foster City, Calif; https://www.appliedbiosystems.com/catalog/). Quantitative real-time PCR for the detection of *GADD34* was performed with QuantiTect SYBR Green Kit (Qiagen, Inc) with the following primers: *GADD34*: forward, ATCTCCTGAACAGAGTCAAGCAGCCCAGAG; reverse, TAGCCACCACCTCCCCAAGCCTCTTATCAG; *GAPDH*: forward, CATCAACGACCCCTTCATTGACCTCAACTA; reverse, TCCACGATGCCAAAGTTGTCATGGATGACC. Quantitative real-time PCR was performed with an ABI PRISM 7000 Sequence Detection System (Applied Biosystems) by the relative standard curve method. The reaction was performed at 50°C for 2 minutes and 95°C for 10 minutes, followed by 40 cycles at 95°C for 15 seconds and 60°C for 1 minute. The amount of each product was determined from the relative standard curves constructed with serial dilutions of the control cDNA.

Real-Time PCR Microarray Analysis

We isolated RNA from the hearts of WT and CHOP-deficient mice at 4 weeks after TAC or sham operation. Then, the synthesis of cDNA and comparison of relative gene expressions for 15 Bcl2 family members were performed with the RT² First Strand Kit and a mouse PCR array (Superarray Bioscience Corp, Frederick, Md). Samples from 3 sham-operated and 3 pressure-overloaded hearts at 4 weeks after operation were compared in WT and CHOP-deficient mice. The average cycle threshold (Ct) was calculated for each Bcl2 family gene and the housekeeping genes (GAPDH and actin), and the ΔCt ($Ct_{\text{Bcl2 family gene}} - Ct_{\text{average of GAPDH and actin}}$) was determined.[22] The values were expressed as the $2^{-\Delta Ct}$, and data of sham-operated and pressure-overloaded hearts were analyzed with $2^{-\Delta\Delta Ct}$ method.[22]

Immunoblotting Analysis

Immunoblotting analysis was performed as described previously.[19] The mitochondrial fraction was extracted from mouse hearts with a Mitochondria Extraction Kit (Imgenex Corp, San Diego, Calif) according to the manufacturer's protocol.

Apoptotic Cell Assay

The terminal deoxynucleotidyl transferase dUTP nick-end labeling (TUNEL) assay was performed as described previously.[9] The number of TUNEL-positive cells was expressed as a percentage of total cells.

Table 1. Clinical Characteristics of 15 Patients With Heart Failure

						Echocardiographic Findings		
Patient	Age, y	Gender	Diagnosis	BNP, pg/mL	NYHA Class	LVEF, %	LVDd, mm	LVDs, mm
1	68	M	ICM	370	IV	33	100	88
2	50	F	DCM	417	IV	32	70	62
3	40	M	DCM	450	III	24	96	87
4	72	M	DCM	310	III	26	91	82
5	67	M	DCM	313	III	24	85	77
6	56	M	ICM	55	III	27	70	63
7	52	M	DCM	1711	IV	25	95	86
8	53	M	DCM	331	III	30	91	81
9	50	M	DCM	1610	IV	17	88	82
10	61	M	DCM	1030	III	12	81	77
11	48	M	DCM	800	IV	19	93	86
12	62	M	DCM	570	III	32	78	69
13	54	M	ICM	321	III	39	74	64
14	66	F	DCM	582	III	33	76	67
15	58	M	DCM	1736	IV	26	82	74

BNP indicates brain-type natriuretic peptide; NYHA, New York Heart Association; LVEF, LV ejection fraction; LVDd, LV end-diastolic dimension; LVDs, LV end-systolic dimension; ICM, ischemic cardiomyopathy; and DCM, dilated cardiomyopathy.

Statistical Analysis

Data are shown as mean±SEM when normally distributed and as median and interquartile range when nonnormally distributed. The Mann-Whitney *U* test was used to compare the levels of *ATF4*, *BiP*, and *CHOP* mRNA between control and failing hearts. The results of echocardiographic parameters, quantitative analysis of immunoblotting, and quantitative real-time PCR were compared by 2-way ANOVA followed by the Bonferroni procedure as a posthoc test. Real-time PCR microarray data were analyzed by the $2^{-\Delta\Delta Ct}$ method with RT^2 profiler PCR array data analysis software (http://www.superarray.com/pcrarraydataanalysis.php). For all analyses, values of $P<0.05$ were accepted as statistically significant. The authors had full access to and take full responsibility for the integrity of the data. All authors have read and agree to the manuscript as written.

Results

Activation of ER Stress Signaling in Failing Human Hearts

ER stress leads to morphological development of the ER and induces the unfolded protein response that increases the expression of ER chaperones such as BiP.[7,8] The *BiP* mRNA level was significantly higher in the hearts of 15 patients with heart failure (Table 1) compared with the 6 control subjects (Figure 1A). Increased expression of this ER-resident chaperone indicates that ER stress occurs in failing human hearts. *ATF4*, a transcriptional factor that regulates CHOP expression,[1,2] and *CHOP* mRNA levels were also significantly higher in the failing human hearts compared with control hearts (Figure 1B and 1C).

Attenuation of Cardiac Hypertrophy and Dysfunction Induced by Pressure Overload in CHOP-Deficient Mice

Because CHOP is involved in ER-initiated apoptotic signaling and was markedly induced in failing human hearts, we investigated its pathophysiological role in the development of heart failure. WT and CHOP-deficient mice were subjected to pressure overload by TAC. There were no significant differences in baseline body weight (23.2±0.1 versus 23.4±0.1 g) and hemodynamic parameters, including heart rate (649±10 versus 652±12 bpm) and systolic blood pressure (112±4

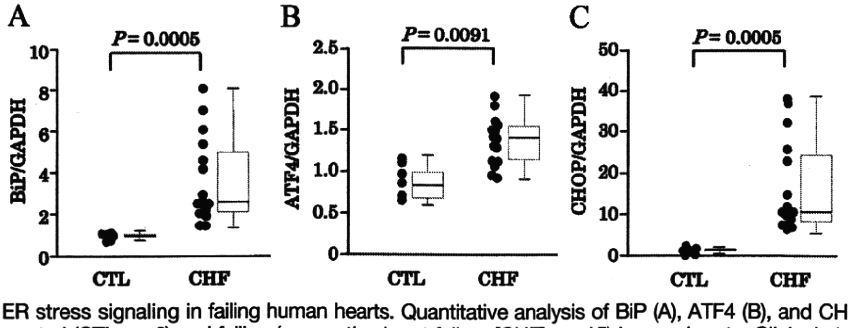

Figure 1. Activation of ER stress signaling in failing human hearts. Quantitative analysis of BiP (A), ATF4 (B), and CHOP (C) mRNA by quantitative real-time PCR in control (CTL; n=6) and failing (congestive heart failure [CHF]; n=15) human hearts. Clinical characteristics of the 15 patients with heart failure are shown in Table 1. Results of real-time reverse-transcription PCR were normalized by GAPDH expression. The central line in each box denotes the median value; the lower and upper boundaries of the box denote interquartile range; and the lower and upper error bars denote minimum and maximum values, respectively.

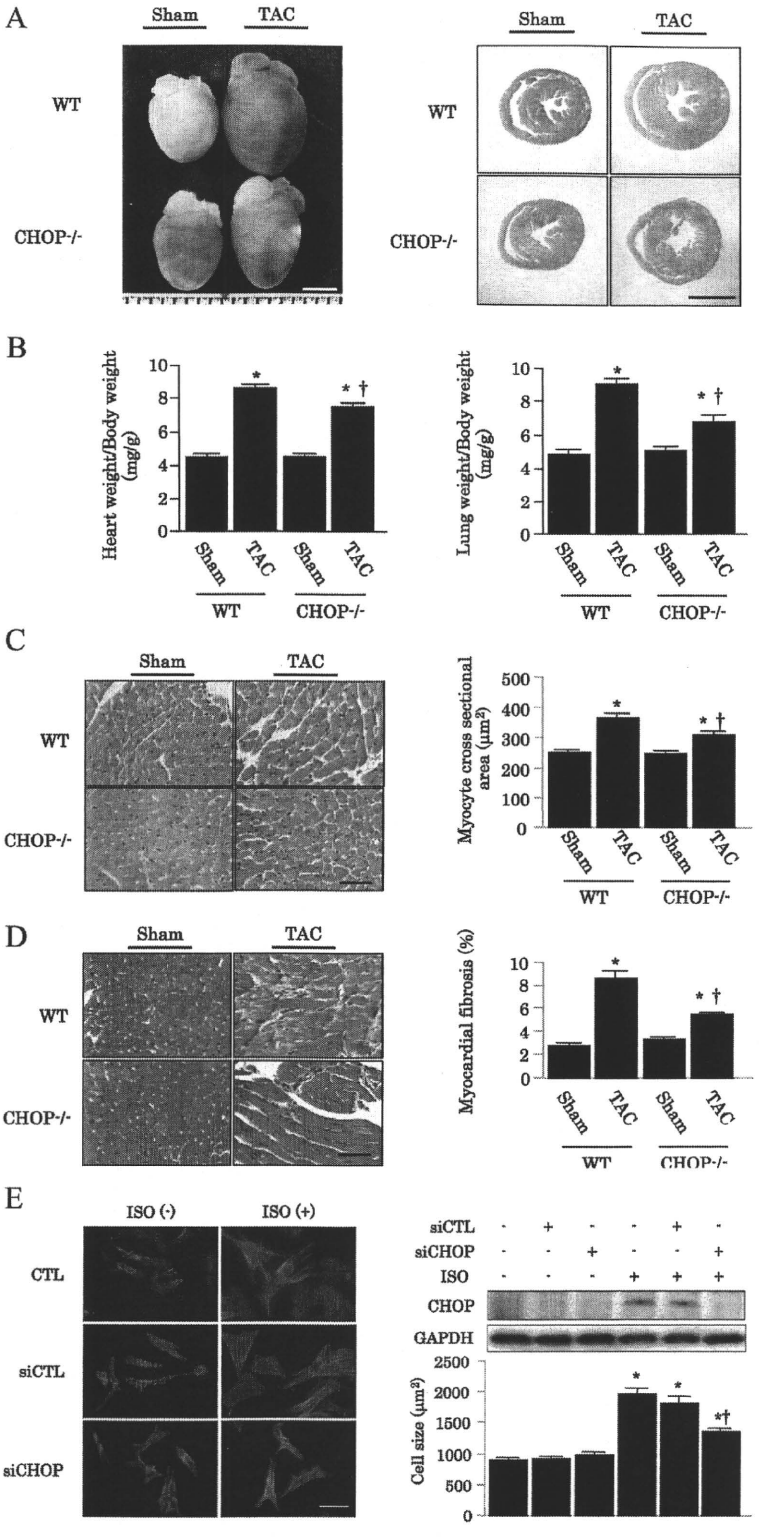

Figure 2. Attenuation of cardiac hypertrophy and dysfunction induced by pressure overload in CHOP-deficient mice. A, left, Representative gross appearance of hearts from WT and CHOP-deficient mice. Scale bars=2.5 mm. Right, Representative hematoxylin and eosin–stained cross sections of LV myocardium from WT and CHOP-deficient mice. Scale bars=2.5 mm. B, Ratios of heart weight to body weight (left) and lung weight to body weight (right) of WT mice (n=16) and CHOP-deficient mice (n=15). C, Representative pictures of myocardium with hematoxylin and eosin stain (left) and quantitative analysis of myocyte cross-sectional area (right). Bar=50 μm. D, Representative pictures of myocardium with Masson trichrome stain (left) and quantitative analysis of cardiac fibrosis (right). Bar=50 μm. *†$P<0.05$ vs WT mice at 4 weeks after sham operation and TAC, respectively. E, Representative pictures showing cultured rat neonatal cardiomyocytes stained with rhodamine-phalloidin (left), representative immunoblotting of CHOP (top right), and quantitative analysis of cell size (bottom right). Cardiomyocytes were treated with siRNA for CHOP (siCHOP) or firefly luciferase from Photinus pyralis (siCTL) as a negative control (60 nmol/L) 4 hours after cardiomyocyte isolation. The immunoblotting and histological analyses were performed 24 hours after treatment with isoproterenol (ISO; 10 μmol/L). *†$P<0.05$ vs control (CTL) and isoproterenol treatments, respectively.

versus 111±3 mm Hg), between WT mice and CHOP-deficient mice. On gross examination, CHOP-deficient mice showed less enlargement of the heart compared with WT mice at 4 weeks after TAC (Figure 2A). The ratios of heart weight to body and lung weight to body weight at 4 weeks after TAC were both significantly smaller in CHOP-deficient mice than in WT mice (Figure 2B). On microscopic examination, CHOP-deficient mice showed less cardiac hypertrophy (Figure 2C) and cardiac fibrosis (Figure 2D) compared with WT mice at 4 weeks after TAC. In cultured rat neonatal cardiomyocytes, the knockdown of *CHOP* by siRNA targeting *CHOP* decreased CHOP protein levels by 80% and significantly attenuated the increase in cell size in response to isoproterenol (Figure 2E).

Table 2. Echocardiographic Parameters in WT and CHOP-Deficient Mice at 4 and 8 Weeks After Sham Operation or TAC

	WT			CHOP$^{-/-}$		
Parameters	Sham (n=8)	TAC at 4 wk (n=8)	TAC at 8 wk (n=4)	Sham (n=6)	TAC at 4 wk (n=9)	TAC at 8 wk (n=3)
LVDd, mm	2.79±0.06	3.48±0.06*	4.38±0.52*	2.85±0.05	3.21±0.05*	3.67±0.24*‡
LVDs, mm	1.07±0.03	2.30±0.07*	3.50±0.68*	1.08±0.02	1.85±0.05*†	2.21±0.17*‡
LVPW, mm	0.64±0.02	0.88±0.02*	0.94±0.03*	0.64±0.03	0.80±0.02*†	0.87±0.04*
LVFS, %	60.7±1.1	35.0±1.0*	22.3±6.9*	62.2±0.9	42.6±1.1*†	39.8±0.8*‡
LVEF, %	91.4±0.6	63.4±2.7*	43.5±11.6*	91.8±0.5	74.6±1.1*†	71.2±1.2*‡
LV mass, mg	46.3±2.4	86.7±2.9*	111.8±7.5*	46.6±2.4	71.4±2.5*†	89.7±10.2*‡

LVDd indicates LV end-diastolic dimension; LVDs, LV end-systolic dimension; LVPW, LV posterior wall thickness; LVFS, LV fractional shortening; and LVEF, LV ejection fraction. Results are presented as mean±SEM.

*P<0.05 versus WT sham operation.

†P<0.05 versus WT TAC at 4 weeks.

‡P<0.05 versus WT TAC at 8 weeks.

Echocardiography revealed that the baseline left ventricular (LV) end-diastolic and systolic dimensions were not significantly different between WT mice and CHOP-deficient mice (Table 2). However, both the LV end-diastolic and end-systolic dimensions were significantly smaller in CHOP-deficient mice than in WT mice at 4 and 8 weeks after TAC (Table 2). Moreover, LV posterior wall thickness and calculated LV mass in CHOP-deficient mice were smaller than in WT mice. These findings suggest that CHOP plays an important role in the development of cardiac hypertrophy and failure by pressure overload in mice.

ER Stress Signaling in Pressure-Overloaded Hearts of WT and CHOP-Deficient Mice

Next, we investigated ER stress signaling in the pressure-overloaded hearts of WT mice and CHOP-deficient mice. We

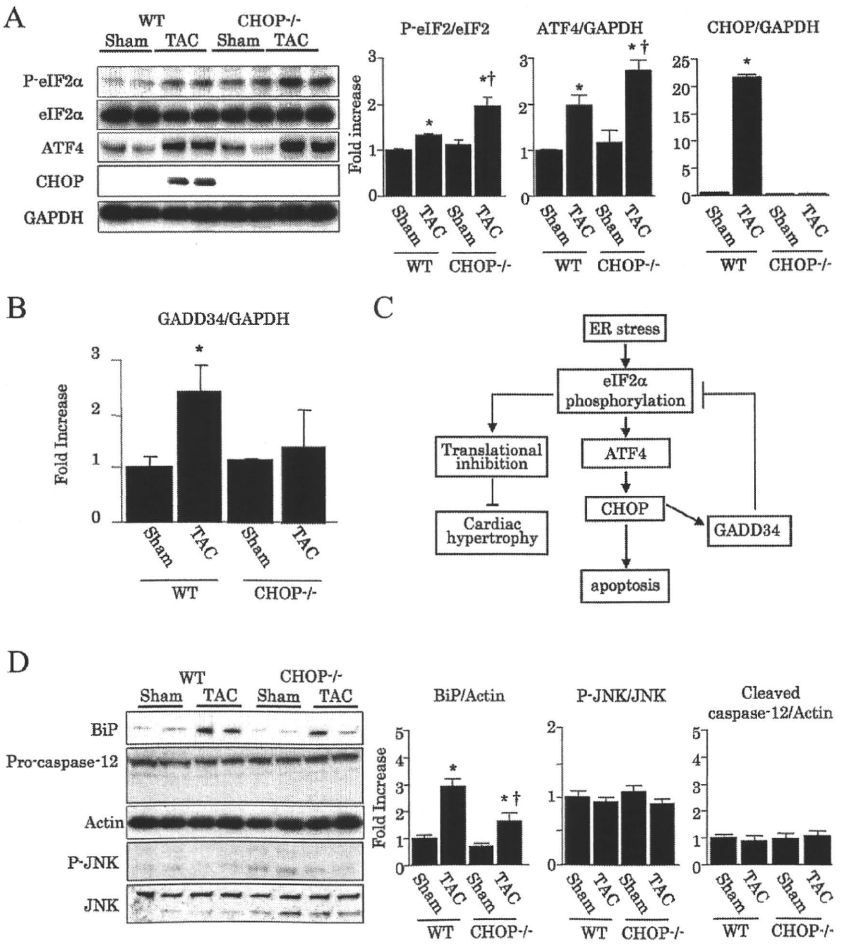

Figure 3. ER stress signaling in pressure-overloaded hearts of WT and CHOP-deficient mice. A, Representative immunoblotting (phospho [P-]-eIF2α, total eIF2α, ATF4, and GAPDH) of ER stress signaling in the hearts of WT and CHOP-deficient mice after sham or TAC operation. The intensity of bands for molecules involved in ER-initiated signaling was quantified from 3 independent experiments by densitometry. B, Quantitative real-time PCR analysis of GADD34 in the hearts of WT and CHOP-deficient mice after sham or TAC operation. C, Schematic diagram of CHOP ablation to attenuate cardiac hypertrophy and apoptosis. D, Representative immunoblotting analysis of ER-initiated apoptosis regulatory proteins in the hearts of WT and CHOP-deficient mice after sham or TAC operation. The intensity of bands for Bip and ER-initiated apoptosis regulatory proteins was quantified from 4 independent experiments by densitometry. Quantitative analysis showed the induction of BiP and CHOP but no increase in caspase-12 cleavage or JNK phosphorylation in the hearts of WT mice after TAC. Results are presented as mean±SEM. *†P<0.05 vs WT mice at 4 weeks after sham operation and TAC, respectively.

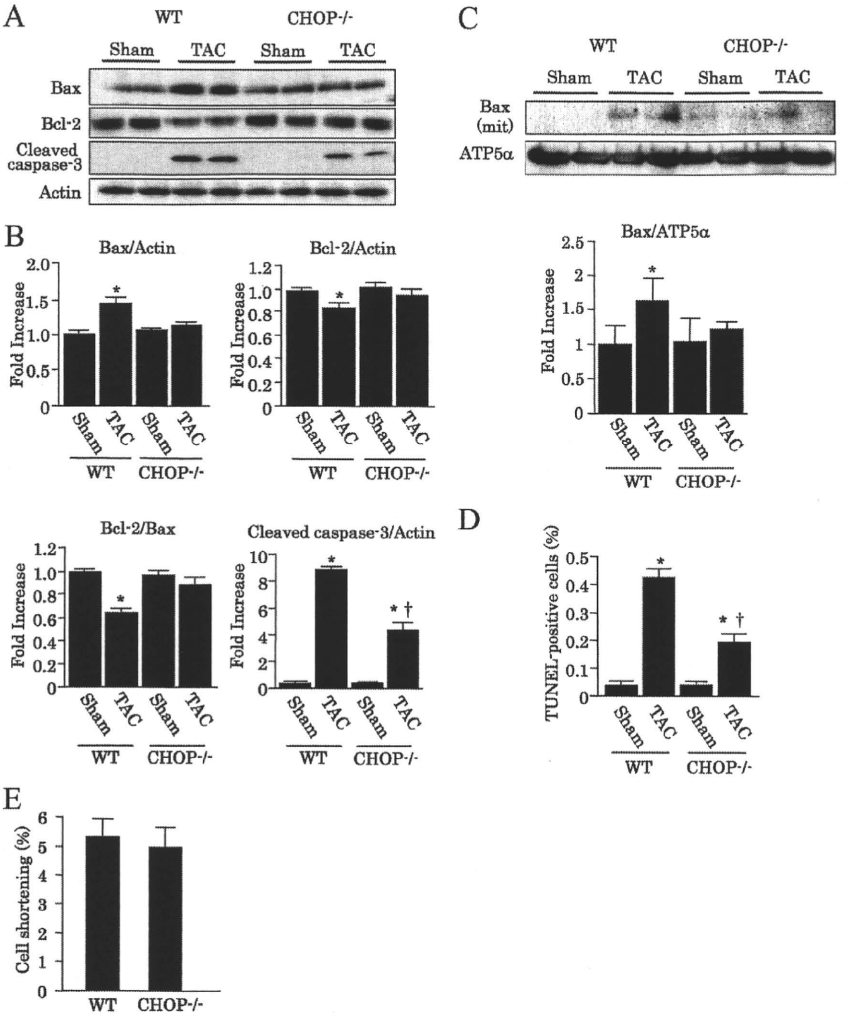

Figure 4. Bcl2 and Bax in pressure-overloaded hearts of WT and CHOP-deficient mice. A, Representative immunoblotting analysis of Bcl2 and Bax in the hearts of WT and CHOP-deficient mice. B, The intensity of bands was quantified from 4 independent experiments by densitometry. Bax protein levels were increased and Bcl2 protein levels were decreased by pressure overload in the hearts of WT mice, whereas Bax and Bcl2 protein levels were not significantly altered in CHOP-deficient mice. A decrease in the Bcl2/Bax ratio was seen in the hearts of WT mice but not CHOP-deficient mice as a result of pressure overload. The level of cleaved caspase-3 was significantly lower in the pressure-overloaded hearts of CHOP-deficient mice than in WT mice. C, Representative immunoblotting and quantitative analysis of mitochondrial Bax protein levels. Translocation of Bax to the mitochondria after TAC was significantly lower in CHOP-deficient mice than in WT mice. The intensity of bands was quantified from 4 independent experiments by densitometry. D, TUNEL staining of the hearts of WT (n=4) and CHOP-deficient (n=4) mice. TUNEL-positive cells were quantified by examination of 3000 nuclei from 10 randomly selected fields per heart. After TAC, the number of TUNEL-positive cells was significantly lower in CHOP-deficient mice than in WT mice. E, Cell shortening of isolated adult cardiomyocytes from WT and CHOP-deficient mice. Results are presented as mean±SEM. *†$P<0.05$ vs WT mice at 4 weeks after sham operation and TAC, respectively.

found that phosphorylation of eIF2α and expression of ATF4, either of which is an upstream signal of CHOP, were increased in hearts after TAC compared with those after sham operation in WT mice (Figure 3A). Expression of CHOP and its downstream target GADD34 was also increased by pressure overload in WT mice (Figure 3A and 3B). CHOP directly activates GADD34, which negatively regulates the phosphorylation of eIF2α and thus increases protein synthesis.[3,23,24] Consistently, in the hearts of CHOP-deficient mice, the increase in GADD34 caused by pressure overload was blunted, which led to enhanced phosphorylation of eIF2α and increased ATF4 (Figure 3A through 3C).

Among the factors involved in ER-initiated apoptotic signaling, caspase-12 or JNK was not activated by pressure overload in the hearts of WT and CHOP-deficient mice at 4 weeks after TAC (Figure 3D). This result was consistent with our previous findings.[9]

Bcl2 Family Genes in Sham-Operated and Pressure-Overloaded Hearts of WT and CHOP-Deficient Mice

The total Bax protein level was increased and the Bcl2 protein level was decreased in the pressure-overloaded hearts of WT mice, leading to a reduction in the Bcl2/Bax ratio (Figure 4A and 4B). We also observed an increase in Bax protein in the mitochondrial fraction from pressure-overloaded hearts of WT mice (Figure 4C). Furthermore, caspase-3 was activated and the number of TUNEL-positive cells was increased in pressure-overloaded hearts of WT mice (Figure 4A and 4D). In contrast, the levels of Bcl2, total Bax, and mitochondrial Bax protein in the hearts of CHOP-deficient mice with pressure overload did not differ from those in sham-operated mice (Figure 4A through 4C). The level of cleaved caspase-3 was lower and the number of TUNEL-positive cells was smaller in the hearts of CHOP-deficient mice with pressure overload compared with WT mice (Figure 4D). In the isolated adult cardiomyocyte from WT and CHOP-deficient mice, there were no significant differences in cardiac contractility under pacing conditions (Figure 4E and the online-only Data Supplement). These findings indicate that CHOP, a transcription factor involved in ER-initiated apoptotic signaling, has a role in mitochondria-dependent apoptosis in hearts subjected to pressure overload.

Finally, we assessed the role of CHOP in the expression of Bcl2 family genes in sham-operated and pressure-overloaded hearts from both WT and CHOP-deficient mice. In sham-operated hearts, none of the 15 Bcl2 family gene expressions showed differences between WT mice and CHOP-deficient mice (Table 3).

Table 3. Gene Expressions of Bcl2 Family Members in Hearts From WT and CHOP-Deficient Mice

	WT			CHOP$^{-/-}$		
Gene	Sham ($2^{-\Delta Ct}\times10^3$)	TAC ($2^{-\Delta Ct}\times10^3$)	TAC/Sham	Sham ($2^{-\Delta Ct}\times10^3$)	TAC ($2^{-\Delta Ct}\times10^3$)	TAC/Sham
Proapoptotic signaling						
Bad	14.3±0.5	15.9±0.1	1.1	15.1±0.2	15.6±1.7	1.0
Bak1	12.8±1.3	17.2±1.8	1.3	13.4±0.5	15.7±1.0	1.2
Bax	20.7±1.8	35.3±2.4	1.7*	22.3±1.2	25.5±1.1	1.1
Bid	0.5±0.0	1.0±0.1	2.0*	0.5±0.0	0.8±0.0	1.4*
Bnip3	264.4±71.2	233.1±10.7	0.9	218.7±20.9	264.2±33.1	1.2
Bnip3l	91.4±1.1	175.4±11.2	1.9*	108.9±10.4	100.6±11.2	0.9
Bok	11.6±0.3	15.0±1.4	1.3*	12.8±0.4	20.9±1.3	1.6*
Antiapoptotic signaling						
Bag1	353.4±36.6	327.5±63.3	0.9	389.7±36.2	456.1±36.8	1.2
Bag3	132.9±20.0	115.8±4.6	0.8	180.1±15.9	167.0±12.4	0.9
Bcl2	5.8±0.5	2.6±0.1	0.5*	5.2±0.2	6.9±1.3	1.3
Bcl2l1	15.0±0.4	10.1±0.8	0.7*	20.1±1.3	16.4±0.8	0.8
Bcl2l10	Undetected	Undetected	...	Undetected	Undetected	...
Bcl2l2	8.7±1.3	5.1±0.5	0.6*	6.3±0.8	4.4±0.4	0.7
Bnip2	60.7±6.2	70.5±5.2	1.2	71.2±1.9	67.8±4.5	1.0
Mcl1	179.6±6.3	276.1±16.2	1.5*	184.9±10.0	237.0±3.3	1.3*

Comprehensive analysis of the gene expressions of 15 Bcl2 family members in the sham-operated or pressure-overloaded hearts from WT and CHOP-deficient mice. Values are expressed as $2^{-\Delta Ct}\times10^3$, and data of sham-operated and pressure-overloaded hearts were analyzed with the $2^{-\Delta\Delta Ct}$ method. Results are presented as mean±SEM.

*$P<0.05$ versus gene expression at 4 weeks after sham operation on corresponding mice (n=3).

Consistent with the alterations in Bcl2 and Bax protein levels, we confirmed that *Bcl2* and *Bax* gene expressions decreased and increased in the pressure-overloaded hearts of WT mice, respectively (Table 3). In addition, we found significant changes in the expressions of other Bcl2 family member genes in pressure-overloaded hearts of WT mice compared with sham-operated ones: an increase in 3 proapoptotic genes (*Bid*, *Bnip3l*, and *Bok*) and 1 antiapoptotic gene (*Mcl1*) and a decrease in 2 antiapoptotic genes (*Bcl2l1* and *Bcl2l2*). In CHOP-deficient mice, except for *Bid*, *Bok*, and *Mcl1*, the expressions of Bcl2 family members did not change in pressure-overloaded hearts compared with sham-operated ones. Interestingly, in addition to *Bcl2* and *Bax*, the expressions of *Bnip3l*, *Bcl2l1*, and *Bcl2l2* in pressure-overloaded hearts differed between WT and CHOP-deficient mice. These findings suggest that ER-initiated apoptotic signaling via CHOP may mediate cardiac myocyte apoptosis by reducing the Bcl2/Bax ratio and/or by altering the expression of other members of the Bcl2 family to trigger mitochondria-initiated apoptosis.

Discussion

The present study confirmed an increase in the expression of BiP, an ER-resident chaperone that facilitates protein folding, in failing human hearts.[9] When ER stress is excessive and/or prolonged, apoptotic signals are initiated by the ER, including induction of CHOP, activation of JNK, and cleavage of caspase-12.[25–27] We confirmed that mRNA levels of ATF4 and CHOP were increased in failing human hearts, suggesting that CHOP could be important for proapoptotic signaling initiated by the ER in human heart failure. Experimental studies showed that CHOP has a critical role in dilated cardiomyopathy caused by aberrant ER quality control and in ischemic neuronal death,[28,29] suggesting that CHOP may be an important molecule in human heart and other diseases.

Therefore, we investigated the pathophysiological role of CHOP in the development of heart failure by using CHOP-deficient mice.[17] We previously demonstrated that cardiac dysfunction is induced in mice by pressure overload at 4 weeks after TAC.[9] Pressure overload caused by TAC increased the ratios of heart weight to body weight and of lung weight to body weight in WT mice, whereas these changes were partially but significantly attenuated in CHOP-deficient mice. In addition, histological analysis revealed that both cardiac hypertrophy and fibrosis in CHOP-deficient mice after TAC were significantly less compared with those in WT mice. Echocardiography demonstrated that LV enlargement and cardiac dysfunction after TAC were attenuated in CHOP-deficient mice compared with WT mice. In cultured rat neonatal cardiomyocytes, we found that the knockdown of CHOP blunted the increase in cell size in response to isoproterenol. These findings suggest that CHOP plays a crucial role in the development of cardiac hypertrophy and heart failure resulting from pressure overload.

CHOP regulates the expression of GADD34, which negatively regulates the phosphorylation of eIF2α. Enhanced phosphorylation of eIF2α reduces protein translation[30] and has been reported to mediate the inhibition of protein synthesis in the rat liver by vasopressin and the rat brain by essential amino acid deficiency.[31,32] Under CHOP-deficient conditions, decreased expression of GADD34 in pressure-overloaded hearts may lead to enhanced phosphorylation of eIF2α and

decreased protein synthesis. Thus, increased phosphorylation of eIF2α in hearts with pressure overload in CHOP-deficient mice is likely to contribute to the prevention of cardiac hypertrophy through the suppression of protein synthesis. Interestingly, pressure overload to hearts specifically activated CHOP but not caspase-12 or JNK. The promoter region of the CHOP gene contains binding sites for all of the major inducers of the unfolded protein response, including ATF4, ATF6, and XBP-1; these transcriptional factors are also involved in the induction of CHOP.[33] It will be important to clarify the selective activation of CHOP in future investigations.

Overexpression of CHOP leads to a decrease in Bcl2 protein, whereas overexpression of Bcl2 blocks CHOP-induced apoptosis.[12,34] In addition, overexpression of CHOP leads to translocation of Bax protein from the cytosol to the mitochondria.[35] Thus, the CHOP-mediated death signal is finally transmitted to the mitochondria, leading to activation of caspase-3.[27,36] In the present study, expression of Bax protein was increased and Bcl2 protein was decreased in the hearts of WT mice after TAC, consistent with previous data.[37] In contrast, these changes in apoptosis-regulating proteins did not occur in hearts of CHOP-deficient mice. These findings suggest that prolonged pressure overload leads to changes in apoptosis-regulating proteins via a CHOP-dependent pathway. Consequently, caspase-3 cleavage was reduced and the number of TUNEL-positive cells was smaller in the hearts of CHOP-deficient mice compared with WT mice at 4 weeks after TAC. Because there were no significant differences in contractility of isolated cardiomyocytes in WT and CHOP-deficient mice, it was likely that the improvement in cardiac function after TAC in CHOP-deficient mice was due to less apoptotic cell death.

Moreover, we performed real-time PCR microarray analysis for 15 Bcl2 family members. We found that the expressions of Bcl2 family member genes in sham-operated hearts were not significantly different between WT mice and CHOP-deficient mice. In pressure-overloaded hearts of WT mice, several Bcl2 family genes, including 4 proapoptotic genes and 4 antiapoptotic genes, were altered. Clarification of the role of each Bcl2 family gene in the development of heart failure is needed in our future studies. Interestingly, in addition to *Bcl2* and *Bax*, we found the difference in the expressions of 3 Bcl2 family genes in pressure-overloaded hearts between WT mice and CHOP-deficient mice: *Bnip3l*, *Bcl2l1*, and *Bcl2l2*. Bnip3l, also referred to as Nix, is induced in cardiac hypertrophy and mediates cardiomyocyte apoptosis.[38]

Consistent with this report, the increase in *Bnip3l* expression was blunted in pressure-overloaded hearts of CHOP-deficient mice. Furthermore, expressions of both *Bcl2l1* and *Bcl2l2* were decreased in pressure-overloaded hearts of WT but not CHOP-deficient mice. Bcl2l1 has been reported to be decreased in hypertrophic and failing hearts after pressure overload.[39] Although the role of Bcl2l2 in cardiomyocytes remains unclear, it is thought to play an important protective role in neurons and in the diseased brain.[40] Because the expressions of *Bid*, *Bok*, and *Mcl1* changed in a similar way between WT mice and CHOP-deficient mice, they may not contribute to the differences in cardiac dysfunction between WT mice and CHOP-deficient mice. These findings suggest that ER stress initiates CHOP-dependent apoptotic signaling, which finally leads to activation of mitochondria-dependent apoptotic signaling via several Bcl2 family members and contributes to heart failure induced by pressure overload. However, we need to carefully consider the difference in gene expression because of the small number of samples. Furthermore, because CHOP mediates apoptosis through the perturbation of the cellular redox state by depletion of intracellular glutathione and through protein-protein interactions,[35,41] we also need to consider whether CHOP influences mitochondria-independent apoptosis in failing hearts.

Conclusion

The present findings suggest that CHOP may be a logical target for the development of drugs to prevent cardiac hypertrophy and cardiomyocyte apoptosis in failing hearts.

Acknowledgment

We thank Dr Tomomi Gotoh (Kumamoto University, Kumamoto, Japan) for providing us with CHOP-deficient mice.

Sources of Funding

This study was supported by grants on Scientific Research from the Ministry of Education, Culture, Sports, Science, and Technology (No. 17590731) and a grant from the Japan Cardiovascular Research Foundation (No. 19390220).

Disclosures

None.

References

1. Ron D, Walter P. Signal integration in the endoplasmic reticulum unfolded protein response. *Nat Rev Mol Cell Biol.* 2007;8:519–529.
2. Xu C, Bailly-Maitre B, Reed JC. Endoplasmic reticulum stress: cell life and death decisions. *J Clin Invest.* 2005;115:2656–2664.
3. Marciniak SJ, Yun CY, Oyadomari S, Novoa I, Zhang Y, Jungreis R, Nagata K, Harding HP, Ron D. CHOP induces death by promoting protein synthesis and oxidation in the stressed endoplasmic reticulum. *Genes Dev.* 2004;18:3066–3077.
4. Urano F, Wang X, Bertolotti A, Zhang Y, Chung P, Harding HP, Ron D. Coupling of stress in the ER to activation of JNK protein kinases by transmembrane protein kinase IRE1. *Science.* 2000;287:664–666.
5. Szegezdi E, Fitzgerald U, Samali A. Caspase-12 and ER-stress-mediated apoptosis: the story so far. *Ann N Y Acad Sci.* 2003;1010:186–194.
6. Maron BJ, Ferrans VJ, Roberts WC. Ultrastructural features of degenerated cardiac muscle cells in patients with cardiac hypertrophy. *Am J Pathol.* 1975;79:387–434.
7. Kaufman RJ. Orchestrating the unfolded protein response in health and disease. *J Clin Invest.* 2002;110:1389–1398.
8. Shaffer AL, Shapiro-Shelef M, Iwakoshi NN, Lee AH, Qian SB, Zhao H, Yu X, Yang L, Tan BK, Rosenwald A, Hurt EM, Petroulakis E, Sonenberg N, Yewdell JW, Calame K, Glimcher LH, Staudt LM. XBP1, downstream of Blimp-1, expands the secretory apparatus and other organelles, and increases protein synthesis in plasma cell differentiation. *Immunity.* 2004;21:81–93.
9. Okada K, Minamino T, Tsukamoto Y, Liao Y, Tsukamoto O, Takashima S, Hirata A, Fujita M, Nagamachi Y, Nakatani T, Yutani C, Ozawa K, Ogawa S, Tomoike H, Hori M, Kitakaze M. Prolonged endoplasmic reticulum stress in hypertrophic and failing heart after aortic constriction: possible contribution of endoplasmic reticulum stress to cardiac myocyte apoptosis. *Circulation.* 2004;110:705–712.
10. Song B, Scheuner D, Ron D, Pennathur S, Kaufman RJ. Chop deletion reduces oxidative stress, improves beta cell function, and promotes cell survival in multiple mouse models of diabetes. *J Clin Invest.* 2008;118:3378–3389.
11. Silva RM, Ries V, Oo TF, Yarygina O, Jackson-Lewis V, Ryu EJ, Lu PD, Marciniak SJ, Ron D, Przedborski S, Kholodilov N, Greene LA, Burke RE. CHOP/GADD153 is a mediator of apoptotic death in substantia nigra

dopamine neurons in an in vivo neurotoxin model of parkinsonism. *J Neurochem.* 2005;95:974–986.
12. McCullough KD, Martindale JL, Klotz LO, Aw TY, Holbrook NJ. Gadd153 sensitizes cells to endoplasmic reticulum stress by down-regulating Bcl2 and perturbing the cellular redox state. *Mol Cell Biol.* 2001;21:1249–1259.
13. Jessup M, Brozena S. Heart failure. *N Engl J Med.* 2003;348:2007–2018.
14. Chien KR. Stress pathways and heart failure. *Cell.* 1999;98:555–558.
15. Foo RS, Mani K, Kitsis RN. Death begets failure in the heart. *J Clin Invest.* 2005;115:565–571.
16. MacLellan WR, Schneider MD. Death by design: programmed cell death in cardiovascular biology and disease. *Circ Res.* 1997;81:137–144.
17. Oyadomari S, Koizumi A, Takeda K, Gotoh T, Akira S, Araki E, Mori M. Targeted disruption of the Chop gene delays endoplasmic reticulum stress-mediated diabetes. *J Clin Invest.* 2002;109:525–532.
18. Liao Y, Takashima S, Zhao H, Asano Y, Shintani Y, Minamino T, Kim J, Fujita M, Hori M, Kitakaze M. Control of plasma glucose with alpha-glucosidase inhibitor attenuates oxidative stress and slows the progression of heart failure in mice. *Cardiovasc Res.* 2006;70:107–116.
19. Minamino T, Yujiri T, Terada N, Taffet GE, Michael LH, Johnson GL, Schneider MD. MEKK1 is essential for cardiac hypertrophy and dysfunction induced by Gq. *Proc Natl Acad Sci U S A.* 2002;99:3866–3871.
20. Fu HY, Minamino T, Tsukamoto O, Sawada T, Asai M, Kato H, Asano Y, Fujita M, Takashima S, Hori M, Kitakaze M. Overexpression of endoplasmic reticulum-resident chaperone attenuates cardiomyocyte death induced by proteasome inhibition. *Cardiovasc Res.* 2008;79:600–610.
21. Muraski JA, Fischer KM, Wu W, Cottage CT, Quijada P, Mason M, Din S, Gude N, Alvarez R Jr, Rota M, Kajstura J, Wang Z, Schaefer E, Chen X, MacDonnel S, Magnuson N, Houser SR, Anversa P, Sussman MA. Pim-1 kinase antagonizes aspects of myocardial hypertrophy and compensation to pathological pressure overload. *Proc Natl Acad Sci U S A.* 2008;105:13889–13894.
22. Livak KJ, Schmittgen TD. Analysis of relative gene expression data using real-time quantitative PCR and the 2(-Delta Delta C(T)) Method. *Methods.* 2001;25:402–408.
23. Novoa I, Zeng H, Harding HP, Ron D. Feedback inhibition of the unfolded protein response by GADD34-mediated dephosphorylation of eIF2alpha. *J Cell Biol.* 2001;153:1011–1022.
24. Zhang K, Kaufman RJ. The unfolded protein response: a stress signaling pathway critical for health and disease. *Neurology.* 2006;66:S102–S109.
25. Rasheva VI, Domingos PM. Cellular responses to endoplasmic reticulum stress and apoptosis. *Apoptosis.* 2009;14:996–1007.
26. Oyadomari S, Mori M. Roles of CHOP/GADD153 in endoplasmic reticulum stress. *Cell Death Differ.* 2004;11:381–389.
27. Zinszner H, Kuroda M, Wang X, Batchvarova N, Lightfoot RT, Remotti H, Stevens JL, Ron D. CHOP is implicated in programmed cell death in response to impaired function of the endoplasmic reticulum. *Genes Dev.* 1998;12:982–995.
28. Hamada H, Suzuki M, Yuasa S, Mimura N, Shinozuka N, Takada Y, Suzuki M, Nishino T, Nakaya H, Koseki H, Aoe T. Dilated cardiomyopathy caused by aberrant endoplasmic reticulum quality control in mutant KDEL receptor transgenic mice. *Mol Cell Biol.* 2004;24:8007–8017.
29. Tajiri S, Oyadomari S, Yano S, Morioka M, Gotoh T, Hamada JI, Ushio Y, Mori M. Ischemia-induced neuronal cell death is mediated by the endoplasmic reticulum stress pathway involving CHOP. *Cell Death Differ.* 2004;11:403–415.
30. Harding HP, Novoa I, Zhang Y, Zeng H, Wek R, Schapira M, Ron D. Regulated translation initiation controls stress-induced gene expression in mammalian cells. *Mol Cell.* 2000;6:1099–1108.
31. Kimball SR, Jefferson LS. Mechanism of the inhibition of protein synthesis by vasopressin in rat liver. *J Biol Chem.* 1990;265:16794–16798.
32. Gietzen DW, Ross CM, Hao S, Sharp JW. Phosphorylation of eIF2alpha is involved in the signaling of indispensable amino acid deficiency in the anterior piriform cortex of the brain in rats. *J Nutr.* 2004;134:717–723.
33. Yoshida H, Matsui T, Yamamoto A, Okada T, Mori K. XBP1 mRNA is induced by ATF6 and spliced by IRE1 in response to ER stress to produce a highly active transcription factor. *Cell.* 2001;107:881–891.
34. Matsumoto M, Minami M, Takeda K, Sakao Y, Akira S. Ectopic expression of CHOP (GADD153) induces apoptosis in M1 myeloblastic leukemia cells. *FEBS Lett.* 1996;395:143–147.
35. Gotoh T, Terada K, Oyadomari S, Mori M. hsp70-DnaJ chaperone pair prevents nitric oxide- and CHOP-induced apoptosis by inhibiting translocation of Bax to mitochondria. *Cell Death Differ.* 2004;11:390–402.
36. Breckenridge DG, Germain M, Mathai JP, Nguyen M, Shore GC. Regulation of apoptosis by endoplasmic reticulum pathways. *Oncogene.* 2003;22:8608–8618.
37. Condorelli G, Morisco C, Stassi G, Notte A, Farina F, Sgaramella G, de Rienzo A, Roncarati R, Trimarco B, Lembo G. Increased cardiomyocyte apoptosis and changes in proapoptotic and antiapoptotic genes bax and bcl-2 during left ventricular adaptations to chronic pressure overload in the rat. *Circulation.* 1999;99:3071–3078.
38. Yussman MG, Toyokawa T, Odley A, Lynch RA, Wu G, Colbert MC, Aronow BJ, Lorenz JN, Dorn GW, II. Mitochondrial death protein Nix is induced in cardiac hypertrophy and triggers apoptotic cardiomyopathy. *Nat Med.* 2002;8:725–730.
39. Sharma AK, Dhingra S, Khaper N, Singal PK. Activation of apoptotic processes during transition from hypertrophy to heart failure in guinea pigs. *Am J Physiol Heart Circ Physiol.* 2007;293:H1384–1390.
40. Zhu X, Wang Y, Ogawa O, Lee HG, Raina AK, Siedlak SL, Harris PL, Fujioka H, Shimohama S, Tabaton M, Atwood CS, Petersen RB, Perry G, Smith MA. Neuroprotective properties of Bcl-w in Alzheimer disease. *J Neurochem.* 2004;89:1233–1240.
41. Ron D, Habener JF. CHOP, a novel developmentally regulated nuclear protein that dimerizes with transcription factors C/EBP and LAP and functions as a dominant-negative inhibitor of gene transcription. *Genes Dev.* 1992;6:439–453.

CLINICAL PERSPECTIVE

Heart failure is a major and growing public health problem worldwide. Although cardiac hypertrophy is a risk factor for the development of heart failure, it is largely unknown how prolonged cardiac hypertrophy causes heart failure. Recently, accumulating evidence has demonstrated that a number of diseases, including neurodegenerative diseases and diabetes mellitus, are associated with the impairment of protein folding in the endoplasmic reticulum (ER). The ER responds to stress by upregulating ER chaperones or attenuating global protein synthesis, but prolonged and/or excess ER stress leads to apoptosis. Here, we provide evidence that C/EBP homologous protein (CHOP), a transcriptional factor that mediates ER-initiated apoptotic cell death, and the ER chaperone were elevated in human failing heart samples, suggesting that ER stress is induced human failing hearts. Pressure overload induced cardiac hypertrophy and failure, along with increased expression in the ER chaperone and CHOP in mice heart. Interestingly, CHOP-deficient mice showed less cardiac hypertrophy and better cardiac function after pressure overload. One possible mechanism for reduced cardiac hypertrophy was enhanced phosphorylation of eukaryotic translation initiation factor 2α, which reduces protein translation and is negatively regulated by CHOP, in pressure-overloaded hearts of CHOP-deficient mice. Furthermore, CHOP decreased Bcl2 protein levels and other Bcl2 family members in cardiomyocytes, suggesting that the ER-mitochondria pathway would play an important role in cell death in pressure-overloaded hearts. In conclusion, the present findings suggest that CHOP may be a logical target for development of drugs to prevent cardiac hypertrophy and cardiomyocyte cell death in failing hearts.

THE JOURNAL OF BIOLOGICAL CHEMISTRY VOL. 285, NO. 41, pp. 31337–31347, October 8, 2010

Isoform-specific Intermolecular Disulfide Bond Formation of Heterochromatin Protein 1 (HP1)*[S]

Received for publication, June 19, 2010, and in revised form, July 26, 2010 Published, JBC Papers in Press, August 1, 2010, DOI 10.1074/jbc.M110.155788

Shuichiro Higo[‡], Yoshihiro Asano[‡§¶], Hisakazu Kato[§], Satoru Yamazaki[¶], Atsushi Nakano[‡], Osamu Tsukamoto[¶], Osamu Seguchi[¶], Mitsutoshi Asai[‡], Masanori Asakura[¶], Hiroshi Asanuma[¶], Shoji Sanada[‡], Tetsuo Minamino[‡], Issei Komuro[‡], Masafumi Kitakaze[¶], and Seiji Takashima[‡§1]

From the Departments of [‡]Cardiovascular Medicine and [§]Molecular Cardiology, Osaka University Graduate School of Medicine, Suita, Osaka 565-0871 and the [¶]Department of Cardiovascular Medicine, National Cardiovascular Center, Suita, Osaka 565-8565, Japan

Three mammalian isoforms of heterochromatin protein 1 (HP1), α, β, and γ, play diverse roles in gene regulation. Despite their structural similarity, the diverse functions of these isoforms imply that they are additionally regulated by post-translational modifications. Here, we have identified intermolecular disulfide bond formation of HP1 cysteines in an isoform-specific manner. Cysteine 133 in HP1α and cysteine 177 in HP1γ were involved in intermolecular homodimerization. Although both HP1α and HP1γ contain reactive cysteine residues, only HP1γ readily and reversibly formed disulfide homodimers under oxidative conditions. Oxidatively dimerized HP1γ strongly and transiently interacted with TIF1β, a universal transcriptional co-repressor. Under oxidative conditions, HP1γ dimerized and held TIF1β in a chromatin component and inhibited its repression ability. Our results highlight a novel, isoform-specific role for HP1 as a sensor of the cellular redox state.

Heterochromatin protein 1 (HP1) was originally characterized as an abundant protein that binds pericentric heterochromatin (1). HP1 acts as a scaffold-like molecule, which is composed of two conserved domains as follows: the chromodomain (CD)[2] and the chromoshadow domain (CSD). The variable hinge region separates these two domains (2). The CD recognizes methylated lysine 9 of histone H3 (H3K9), which recruits HP1 to specific sites within the genome (3–5). The CSD promotes HP1 homodimer formation and provides a surface for interaction with a variety of other chromatin proteins (6, 7). Although genetic experiments previously revealed that HP1 works as a repressor of gene activation by propagation of a heterochromatin structure, emerging evidence has elucidated its diverse functions other than gene silencing (8). Some of these functions are regulated in an isoform-specific manner (9).

In vertebrates, three isoforms of HP1 exist as follows: α, β, and γ, all of which share highly conserved domains. Tethering any HP1 isoform upstream of a promoter equally triggers gene silencing concomitant with local chromatin condensation and an increase in H3K9 methylation (10–12), indicating their common silencing ability. However, nonredundant functions (13, 14), different binding affinities to other proteins (15–17) and different localizations in tissues (18, 19), of these three HP1 isoforms imply that α, β, and γ are functionally diverse. Furthermore, recent evidence clarified apparently opposite functions of HP1 isoforms, *e.g.* a role in transcriptional activation or in transcriptional elongation (20, 21). One mechanism that could account for such functional diversity of HP1 isoforms is post-translational modification, which could cause conformational changes in the molecule. In fact, reversible modifications of HP1 (*e.g.* phosphorylation) can modulate its function in response to various stimuli or cellular environments, suggesting an active role for HP1 beyond its known function as a marker of heterochromatin (17, 22). However, the precise modulatory mechanism across three HP1 isoforms that leads to functional differences remains to be elucidated.

Here, we identified isoform-specific disulfide bond formation as a novel post-translational modification of HP1. We analyzed the biochemical and functional characteristics of this oxidative modification. These data may offer a new insight into a novel role for HP1 during the cellular response to oxidative stress.

EXPERIMENTAL PROCEDURES

Materials—We used the following commercially available materials for Western blotting: anti-HP1α (H2164, Sigma; 19s2, Millipore); anti-HP1β (MAB3448, Chemicon); anti-HP1γ (42s2, Millipore); anti-FLAG M2-peroxidase antibody (Sigma); anti-histone H3 (ab1791, Abcam); anti-GAPDH (MAB374, Chemicon); and anti-TIF1β (4123, Cell Signaling). We also used anti-FLAG M2 affinity gel for immunoprecipitation. We used menadione (Sigma), H_2O_2 (Wako), and hydroxytamoxifen (4-OHT) (Sigma) for cell treatment.

Cell Fractionation—Cells were lysed with hypotonic lysis buffer (10 mM HEPES, pH 7.9, 1.5 mM $MgCl_2$, and 10 mM KCl) with 0.5% Nonidet P-40 and centrifuged at 20,000 × *g* for 5 min.

* This work was supported by grants-in-aid from the Ministry of Health, Labor, and Welfare of Japan, grants-in-aid from the Ministry of Education, Culture, Sports, Science, and Technology of Japan, grants from the Japan Heart Foundation, grants from the Japan Cardiovascular Research Foundation, a grant from the Japan Society for the Promotion of Science, Mochida Memorial Foundation for Medical and Pharmaceutical Research, Japan Medical Association, Japan Incurable Diseases Research Foundation, Osaka Medical Research Foundation for Incurable Diseases, Suzuken Memorial Foundation, and Japan China Medical Association.

[S] The on-line version of this article (available at http://www.jbc.org) contains supplemental Figs. S1–S4, "Experimental Procedures," and additional references.

[1] To whom correspondence should be addressed. Tel.: 81-6-6879-3472; Fax: 81-6-6879-3473; E-mail: takasima@medone.med.osaka-u.ac.jp.

[2] The abbreviations used are: CD, chromodomain; CSD, chromoshadow domain; HUVEC, human umbilical vein endothelial cell; 4-OHT, hydroxytamoxifen.

The supernatant was collected as the cytosolic fraction. Extraction buffer (20 mM HEPES, pH 7.9, 1.5 mM $MgCl_2$, 0.42 M NaCl, 0.2 mM EDTA, 25% glycerol) was added to the pellet, and ultrasonic agitation was performed (30-s sonication with 30-s interval, 4–6 times at 0 °C; Bioruptor, CosmoBio). The suspension was incubated for 15 min at 4 °C and centrifuged at 20,000 × *g* for 10 min. The supernatant was collected as the nuclear extract.

Column Chromatography—For anion exchange, whole cells were lysed with buffer A (20 mM Tris, pH 8.0, 5% acetonitrile) containing 5 mM EDTA and 1% Nonidet P-40 and incubated at 4 °C for 15 min. The lysate was centrifuged at 20,000 × *g* for 5 min, and the supernatant was filtered and loaded onto an anion-exchange column (Q-Sepharose High Performance, GE Healthcare) pre-equilibrated with buffer A. After unbound samples were washed, protein was eluted with a linear gradient (0–100%) of buffer B (buffer A with 1.0 M NaCl). For reverse-phase HPLC, purified protein samples and nuclear extracts were prepared with 0.3% trifluoroacetic acid (TFA) and 20% acetonitrile and applied to a phenyl reverse-phase column (4.6 × 250 mm; Nakalai Tesque). Bound proteins were eluted by a segmented linear gradient of increasing concentrations of buffer B (acetonitrile and 0.1% TFA) in buffer A (0.1% TFA) at a flow rate of 0.5 ml/min. Buffer B was increased at a rate of 1.0%/fraction (fast gradient) or 0.2%/fraction (slow gradient). Collected fractions were dried by a centrifugal evaporator and reconstituted with SDS sample buffer with or without 2.5% 2-mercaptoethanol (reducing or nonreducing conditions, respectively).

Triton Extraction—Triton extraction was carried out as described previously with modification (23). Cells were lysed with a hypotonic lysis buffer with 0.5% Nonidet P-40 and centrifuged at 20,000 × *g* for 5 min (as described above). The pellet was lysed in extraction buffer with 0.2% Triton X-100, incubated on ice for 30 min, and centrifuged at 20,000 × *g* for 5 min. The supernatant was kept as a Triton-soluble fraction. The remaining pellet was lysed in SDS sample buffer (250 mM Tris, 5% SDS, and 5% glycerol) with or without 2.5% 2-mercaptoethanol (reducing or nonreducing conditions, respectively), and ultrasonic agitation was performed as described above. After centrifugation at 20,000 × *g* for 5 min, the supernatant was kept as a Triton-insoluble fraction.

RNAi Knockdowns and Generation of HEK293T Stable Cells—Lentiviral particles derived from the pLKO.1-puro-containing shRNA sequence were purchased from the Mission shRNA library (Sigma). The oligonucleotide sequences of the shRNA were as follows: shRNA-6, CGACGTGTAGTGAATGGGAAA; and shRNA-7, GCGTTTCTTAACTCTCAGAAA. Lentiviral particles were used to transduce human umbilical vein endothelial cells (HUVECs) or HEK293T cells in the presence of 8 μg/ml Polybrene. To generate a HEK293T stable cell line, the infected cells were selected with 1 μg/ml puromycin. The stable cells in which HP1γ was almost completely depleted were next transfected with pEF-DEST51 HP1γ-FLAG WT or a C177S mutant (cloned from murine cDNA and resistant to shRNA), and the stable cells were selected with 5 μg/ml blasticidin.

GAL4-luciferase Reporter Assay—pC3-ERHBD-GAL4 or pC3-ERHBD-GAL4-KAP1 (TIF1β) with pGL4.31-PSV40-GAL4UAS were transfected using Lipofectamine 2000 into subconfluent HEK293T stable cells that were passaged 1 day before transfection. After 24 h, 0.04% ethanol or 4-OHT (500 nM) was added to the culture medium. Forty eight h after transfection, luciferase activity was measured by a luminometer (Lumat LB9507). Intranuclear mRNA levels of luciferase were measured as follows. Twenty four h after transfection, 4-OHT (500 nM) was added to the culture medium. Forty eight h after transfection, cells were lysed with a hypotonic lysis buffer with 0.5% Nonidet P-40 and centrifuged at 20,000 × *g* for 5 min (as described above). From the nuclear pellet, total RNA was isolated using RNA-Bee (Cosmo Bio). Total RNA was treated with DNase (Turbo DNA-free, Applied Biosystems) and was reverse-transcribed using a high capacity cDNA reverse transcription kit (Applied Biosystems). Luciferase mRNA levels were measured by real time quantitative PCR (SYBR Green ER, Invitrogen). Firefly luciferase cDNA was amplified using the following primers: 5′-TACCCACTCGAAGACGGGAC-3′ and 5′-ACTCGGCGTAGGTAATGTCCACCTC-3′. Human 18 S ribosomal RNA was measured using the following primers: 5′-GTAACCCGTTGAACCCCATT-3′ and 5′-CCATCCAATCGGTAGTAGCG-3′. The relative levels of luciferase mRNA were normalized to the mRNA levels of 18 S ribosomal RNA.

RESULTS

HP1α Forms Dimers via Disulfide Bonds through Cysteine 133—During purification of HP1α in our previous work (24), we found that endogenous HP1α separates into two peaks by fractionation using reverse-phase HPLC. To confirm this finding, we fractionated whole cell lysates from HEK293T cells using two-step column chromatography (Fig. 1*A*). Endogenous HP1α was eluted at a salt concentration ranging from 0.3 to 0.35 M on a Q-Sepharose anion-exchange column (Fig. 1*D, top panel*). We applied this single peak to a reverse-phase column. After elution with a fast gradient, HP1α was still detected as a single peak (Fig. 1*D, 2nd panel*). However, when eluted with a slow gradient, HP1α separated into two peaks representing a hydrophilic and a hydrophobic form (Fig. 1*D, 3rd panel*). Two other HP1α antibodies against different epitopes also detected both bands (data not shown), suggesting that these were biochemically different forms of HP1α. Even after direct fractionation of the nuclear extract, which includes the bulk of HP1α protein (Fig. 1*B*), endogenous HP1α showed a similar bimodal distribution (Fig. 1*D, 4th panel*). In other primary cells (HUVECs, neonatal rat cardiomyocytes, and rat cardiac fibroblasts), similar bimodal peaks were observed (supplemental Fig. S1). In contrast, recombinant HP1α expressed in *Escherichia coli* (Fig. 1*C*) exhibited only one peak with elution characteristics similar to those of the hydrophilic peak under the same separating condition used for the endogenous protein (Fig. 1*D, bottom panel*). These data suggest that two different forms of HP1α endogenously exist in multiple cell types and that the late-eluted hydrophobic species may be a post-translationally modified form.

To further elucidate the molecular characteristics of these two forms of HP1α, we used recombinant FLAG-tagged HP1α (HP1α-FLAG). As with endogenous HP1α, HP1α-FLAG existed mainly as a nuclear protein (Fig. 1*E*) and exhibited the

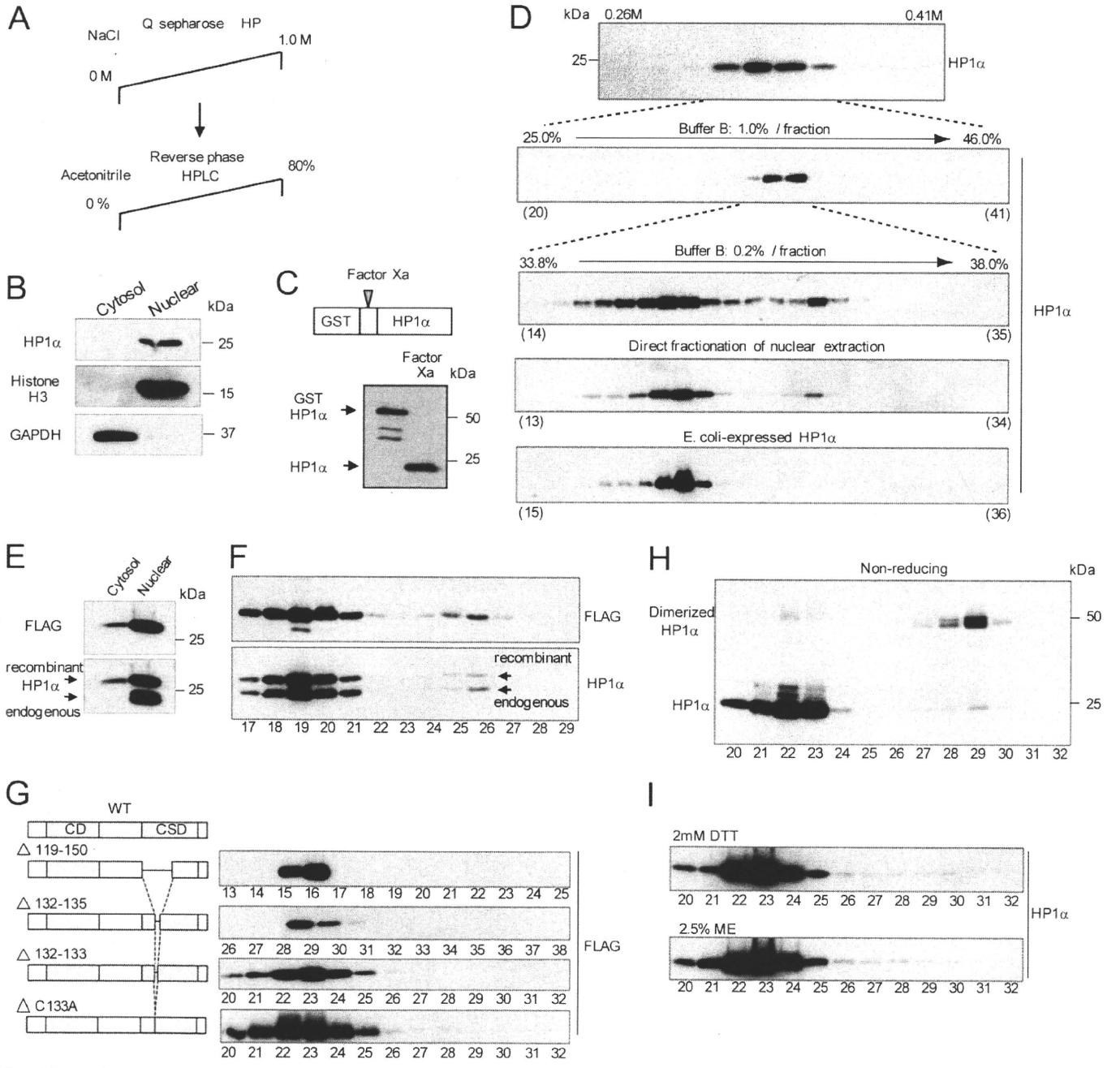

FIGURE 1. **Endogenous HP1α shows a bimodal distribution after protein purification by reverse-phase HPLC.** The late-eluted fraction of HP1α is oxidatively modified to form a disulfide bond. *A*, schematic representation of HP1α purification from cell lysates using sequential column chromatography. *B*, equal quantities of cytosolic and nuclear fractions from HEK293T cells were resolved by SDS-PAGE and probed with the indicated antibodies. *C*, GST-HP1α expressed in *E. coli* was purified and cleaved by Factor Xa (*upper panel*) and detected with anti-HP1α antibody (*lower panel*). *D*, HEK293T cell lysate was fractionated by a Q-Sepharose HP anion-exchange column. Eluted fractions were resolved by reducing SDS-PAGE and probed with anti-HP1α antibody (*top panel*). The *x* axis at the *upper edge* indicates salt concentration. HP1α fractions eluted from the anion-exchange column were next applied to a phenyl reverse-phase column. The fractions were eluted by a fast gradient (buffer B, 1.0% increase of acetonitrile concentration/fraction, *2nd panel from the top*) or by a slow gradient (buffer B, 0.2%/fraction, *3rd panel from the top*). Nuclear extraction from HEK293T cells (*4th panel from the top*) or HP1α purified from *E. coli* (*bottom panel*) was fractionated with the same slow gradient. The eluted fractions were resolved by reducing SDS-PAGE and probed with anti-HP1α antibody. *E*, equal quantities of cytosolic and nuclear fractions from HEK293T cells expressing HP1α-FLAG were resolved by SDS-PAGE and probed with the indicated antibodies. *F*, nuclear extract from HEK293T cells expressing HP1α-FLAG was directly applied to a reverse-phase column, and the eluted fractions were resolved by reducing SDS-PAGE and probed with the indicated antibodies. *G*, diagrams of the representative deletion mutant or point mutant of the HP1α protein during stepwise mutation analysis (*left column*). Nuclear extractions from HEK293T cells expressing each mutant protein were fractionated by reverse-phase HPLC, resolved by SDS-PAGE, and probed with anti-FLAG antibody (*right column*). *H*, endogenous HP1α was purified from the HEK293T cell lysate as shown in *A*. The fractions eluted from the reverse-phase column were resolved by SDS-PAGE under nonreducing conditions and probed with anti-HP1α antibody. *I*, nuclear extract from HEK293T cells was incubated with 2 mM DTT or 2.5% 2-mercaptoethanol (*ME*) for 30 min at 4 °C and then applied to a reverse-phase column. The eluted fractions were resolved by SDS-PAGE and probed with anti-HP1α antibody. *D* and *F–I*, the *x* axis at the *lower edge* indicates fraction numbers.

same bimodal distribution after reverse-phase HPLC (Fig. 1*F*). Thus, we concluded that HP1α-FLAG undergoes the same modification as endogenous HP1α, validating the use of the tagged protein for further analysis. Initially, we attempted to detect the specific modification directly by matrix-assisted laser desorption/ionization and time-of-flight mass spectrometry (MALDI-TOF/MS) (supplemental Fig. S2, *A–C*). Although we detected peptide masses from both fractions corresponding to ~75% of the entire HP1α sequence (supplemental Fig. S2*B*), we did not detect any distinct features in the mass spectra under two different digestion conditions (trypsin or Asp-N) (supplemental Fig. S2*C*). We next tried to detect a modified residue by making multiple, stepwise mutations throughout the entire HP1α molecule. We hypothesized that HP1α-FLAG lacking the modified residue would fractionate into a single peak by reverse-phase HPLC. First, we thoroughly screened the CD and hinge region, both of which are reported to be post-translationally modified (17, 22). However, we could not determine any specific amino acid residue from the mutational analysis (supplemental Fig. S2*D*). Second, we screened the CSD (supplemental Fig. S2*E*) and found that a deletion mutant lacking residues 119–150 (Δ119–150) was eluted as a single peak. We further narrowed down the deleted sequence 119–150 and finally found that a mutant in which cysteine 133 (Cys-133) was replaced by alanine (C133A) was eluted as a single peak (Fig. 1*G*). These data suggest that the single cysteine 133 residue is responsible for the separation of the hydrophobic fraction of HP1α.

Among post-translational modifications of cysteine, oxidation is a common feature. The thiol side chain can be oxidized to sulfenic acid (-SOH), sulfenyl amide (–SN), a disulfide bond (–SS–) or an irreversibly oxidized form (25). We examined the electrophoresis pattern of the two separated fractions of HP1α under nonreducing conditions and found that the hydrophobic form of HP1α shifted to a molecular weight twice its size, indicating that this HP1α formed a homodimer (Fig. 1*H*). In contrast, the mobility of the hydrophilic HP1α was unchanged. Because this dimer was nondissociable both under the strong acidic conditions of the reverse-phase HPLC and under the denaturing conditions during SDS-PAGE, it seemed to be linked by a covalent bond. Pretreatment with reducing agents, such as 2 mM DTT or 2.5% 2-mercaptoethanol, completely abolished the hydrophobic fraction (Fig. 1*I*). Taken together, these data suggest that endogenous HP1α dimerizes by intermolecular disulfide bond formation via Cys-133.

HP1α and HP1γ Both Possess an Isoform-specific Cysteine Residue for Disulfide Bond Formation—The sequence identity among the three HP1 isoforms is remarkably high (Fig. 2*A*), with up to 80% homology in the CSD. However, Cys-133 is specific to HP1α and is replaced by a serine in HP1β and HP1γ (highlighted in *red* in Fig. 2*A*). Therefore, we evaluated whether this oxidative modification was specific for HP1α. Endogenous HP1β was fractionated as a single peak by reverse-phase HPLC. However, endogenous HP1γ was isolated as two separate peaks (Fig. 2*B*). Both the hydrophilic and the hydrophobic fractions of HP1γ were eluted independently of those of HP1α suggesting that these two isoforms did not interact with each other during reverse-phase HPLC fractionation. Similar to HP1α, the hydrophobic form of HP1γ also dimerized (Fig. 2*C*). HP1β contains only two cysteines, both of which are conserved among the isoforms (Cys-59 and Cys-160 of HP1α; highlighted in *blue* in Fig. 2*A*). HP1γ has three cysteines, and one of the cysteines, Cys-177, is an isoform-specific residue located in the C terminus of the CSD. This residue is replaced by tyrosine in HP1α and HP1β (highlighted in *red* in Fig. 2*A*). Mutational analysis of these cysteine residues revealed that only isoform-specific Cys-133 of HP1α and Cys-177 of HP1γ were involved in dimerization (Fig. 2*D*). Mutating the corresponding residues of HP1β, Ser-129 (matched to Cys-133 of HP1α) or Tyr-173 (matched to Cys-177 of HP1γ), to cysteines created the late-eluted hydrophobic form (Fig. 2*E*). These hydrophobic forms of HP1β dimerized similarly with HP1α and HP1γ (Fig. 2*F*). The other two HP1β mutants, S141C and S162C, did not form disulfide bonds. Together, these data suggest that even though their overall structures are highly conserved, endogenous HP1α and HP1γ possess isoform-specific cysteine residues involved in the intermolecular disulfide bond formation. These two positions of the disulfide-linked cysteines are structurally sensitive to oxidation within the CSD.

HP1γ Is More Sensitive to Oxidation than HP1α in Vitro—We tested whether the differences in the positions of the modified cysteine residues between HP1α and HP1γ influenced their sensitivity to oxidation *in vitro*. Under mild oxidative conditions, only a low level of dimerized HP1α was detected even after a long exposure to air oxidation (Fig. 3*A*, *left panels*). In contrast, under the same conditions, HP1γ was easily oxidized to form disulfide bonds (Fig. 3*A*, *right panels*). Treatment with DTT reversed the disulfide formation of HP1γ. These data indicate that HP1γ is more sensitive to oxidation and more readily forms a disulfide dimer *in vitro*.

Using purified and oxidized HP1γ-FLAG, the intermolecular disulfide bond was confirmed by MALDI-TOF/MS analysis. The late-eluted dimerized fraction of HP1γ-FLAG was resolved by nonreducing SDS-PAGE, and the excised band was divided into two samples. One sample was reduced, carbamidomethylated with iodoacetamide, and digested by trypsin. The other sample was directly digested without pretreatment. The expected digested peptide, including Cys-177, consisted of the C terminus of HP1γ and lysine residue within the linker peptide (Fig. 3*B*). The mass spectrum peak of 3084.32, which was detected only in the nonreduced sample, corresponded to the estimated mass of the dimeric peptide connected by a disulfide bond via Cys-177 (3084.35) (Fig. 3*C*, *upper panel*). In contrast, the peak at 1600.68, which was detected only in the reduced sample, corresponded to the estimated mass of the monomeric peptide, including carbamidomethylated Cys-177 (1600.71) (Fig. 3*C*, *lower panel*). No other significant mass spectral peaks from the intermolecular disulfide bond were detected.

HP1γ, but Not HP1α, Readily Forms Disulfide Bonds under in Vivo Oxidative Conditions—We assessed whether this oxidative modification was promoted under *in vivo* oxidative conditions using a pro-oxidant agent, 2-methyl-1,4-naphthoquinone (menadione), which caused oxidative stress in cells (Fig. 4*A*) (26). Menadione treatment caused a dose- and time-dependent increase in the disulfide bond formation of HP1γ in COS7 cells (Fig. 4*B*, *left two panels*). The disulfide dimerization of HP1γ

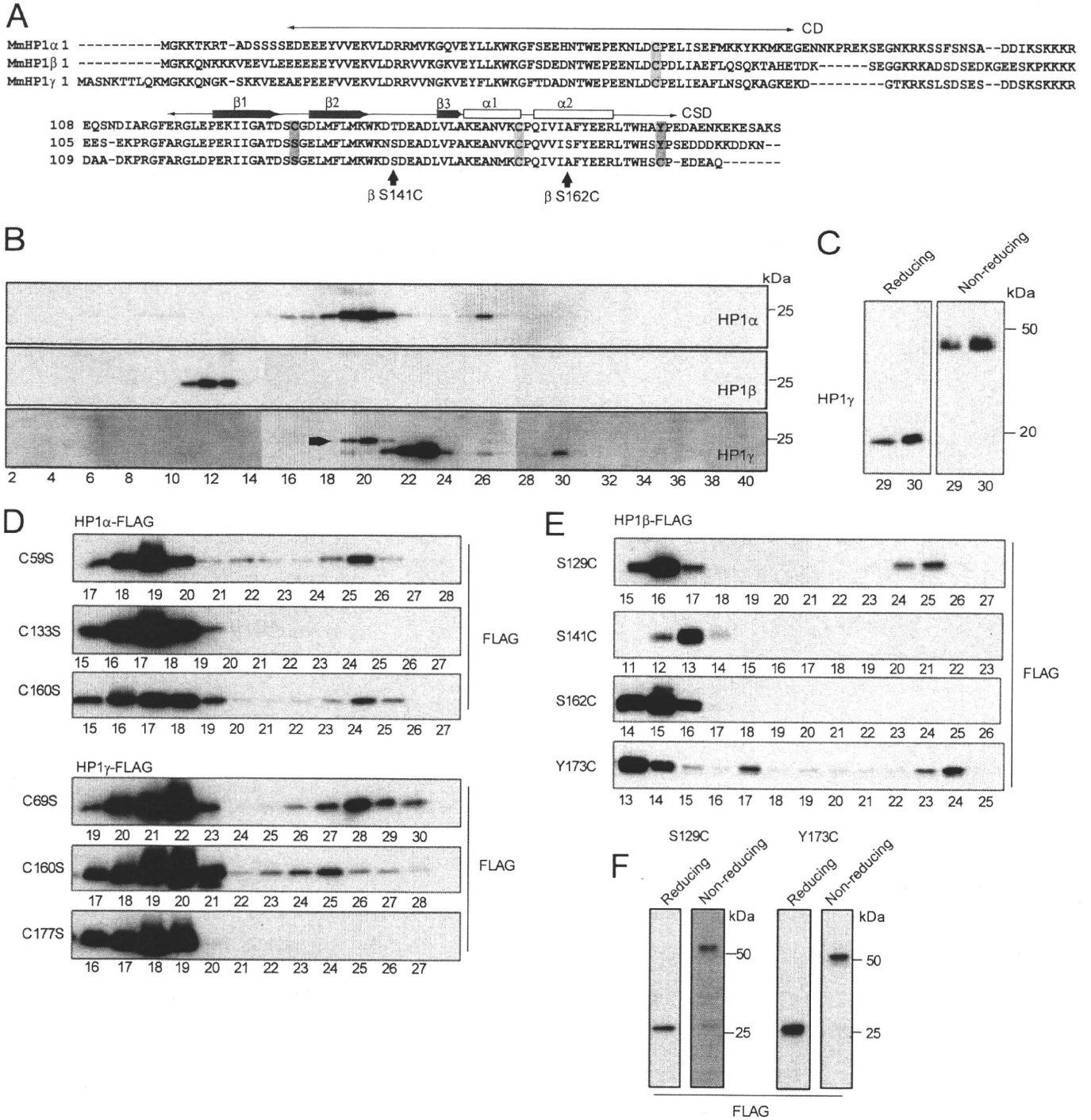

FIGURE 2. **Both HP1α and HP1γ possess isoform-specific cysteine residues that are oxidatively modified to form disulfide bonds.** *A*, amino acid sequence alignment among mouse HP1 isoforms. *Crosswise two-headed arrows* indicate the N-terminal CD and C-terminal CSD. The *bold blue arrow* and *bold white line* along the CSD indicate β-sheet and α-helix, respectively. *Blue highlights* represent the following: two cysteine residues conserved among the HP1 family (Cys-59 and Cys-160; HP1α). *Red highlights* represent the following: position of the cysteine residue specific to HP1α (Cys-133) or HP1γ (Cys-177). The *arrowhead* indicates the position of the mutated HP1β serine residue (shown in *E*). *B*, nuclear extract from HEK293T cells was directly applied to a reverse-phase column, and the eluted fractions were resolved by SDS-PAGE and probed with anti-HP1α, -β, or -γ antibodies. The immunoblotting procedure was performed by consecutive stripping and reprobing with each antibody of the same membrane. The *upper band* of fraction 20 in the *bottom panel* (*arrowhead*) indicates the residual signal from hydrophilic HP1α. *C*, hydrophobic fractions of HP1γ purified from HEK293T cells (as shown in Fig. 1*A*) were resolved by SDS-PAGE under reducing or nonreducing conditions and probed with anti-HP1γ antibody. *D*, nuclear extract from HEK293T cells expressing each HP1α-FLAG (*top three panels*) or HP1γ-FLAG (*bottom three panels*) with a cysteine-to-serine mutation was fractionated by reverse-phase HPLC, resolved by SDS-PAGE, and probed with anti-FLAG antibody. *E*, nuclear extract from HEK293T cells expressing HP1β-FLAG with each serine-to-cysteine or tyrosine-to-cysteine mutation was fractionated by reverse-phase HPLC, resolved by SDS-PAGE, and probed with anti-FLAG antibody. *F*, late-eluted hydrophobic fraction of the HP1β-FLAG mutant (S129C or Y173C) was resolved by reducing or nonreducing SDS-PAGE and probed with anti-FLAG antibody. *B–E*, the *x* axis at the lower edge indicates fraction numbers.